



December 5, 2023

CPSC Staff¹ Statement on: Characterization Methods for Nanomaterial Release During a 3D Printing Process

The report titled “Characterization methods for nanomaterial release during a 3D printing process” describes studies performed by the National Institute of Standards and Technology (NIST). The studies were supported by interagency agreement CPSC-I-15-0017 between the Consumer Product Safety Commission (CPSC) and NIST.

NIST’s Material Measurement Laboratory (MML) conducts measurement science research, provides technical expertise to the development of standards, and performs fundamental and applied research to assure the quality of measurement results. MML staff developed analytical methods to analyze and detect the presence of engineered nanomaterials (multiwalled carbon nanotubes, MWCNTs) in 3D printing materials and to assess the potential for MWCNT release during the printing process. MML staff used advanced microscopic techniques to determine the morphology of particles released during the 3D printing process.

Nanoparticles are of concern because their nanoscale size enables these particles to penetrate to the deep lung when inhaled and potentially move across lung cell walls and become systemically distributed. Published literature from in vivo studies has shown that carbon nanotubes (CNTs, including MWCNTs) and carbon nanofibers (CNF) can cause persistent pulmonary inflammation, granulomatosis, and fibrosis. In addition, immunosuppression, neuroinflammation, and cardiovascular effects, such as endothelial dysfunction, may occur from systemic inflammation in laboratory animals following inhalation exposure to CNTs. While these health effects have been observed in animal studies, epidemiological studies in workplaces involved with CNT/CNF production, use or other related exposure have not shown consistent patterns in the health effects assessed (e.g., respiratory symptoms and illnesses; blood pressure; heart rate; hematology; as well as serum markers of oxidative stress, inflammation, fibrosis, and immunosuppression).

CNTs are known for their mechanical, electrical, and thermal properties. Inherent structural defects in MWCNTs enable strong interactions of the MWCNTs with other polymers, including cross-linking and functionalization. MWCNTs use as additives in 3D printing filaments provides enhanced mechanical strength, thermal stability, and conductivity to the filament and printed product.

NIST noted the market growth of 3D printers such that these printers are widely available at schools, libraries, and home offices. NIST selected two 3D printers that use fused filament fabrication (FFF) technology, the process that operates the more affordable 3D printers used by hobbyists, schools and small businesses. The two 3D printers differed in their design, one was an

¹ This statement was prepared by the CPSC staff, and the attached report was prepared by NIST for CPSC staff. The statement and reports have not been reviewed or approved by, and may not represent the views of, the Commission.

enclosed system with a static heated build plate, while the other was an open frame printer with a mobile heated platform. Commonly used thermoplastic polymer filaments for FFF systems are acrylonitrile butadiene styrene (ABS) and polylactic acid (PLA). NIST chose to analyze a MWCNT ABS composite filament and for comparison, a non-MWCNT ABS filament (“neat ABS filament”) from the same manufacturer. NIST confirmed the ABS matrix polymer via Fourier-transform infrared analysis (FTIR), and the presence and concentration of MWCNTs in the filaments by scanning electron microscopy (SEM) and thermal gravimetric analysis (TGA). NIST observed numerous protruding and embedded MWCNTs in the SEM generated images of the MWCNT ABS filaments. (None were seen in the neat ABS filament.) The estimated mass fraction of MWCNTs in the filament was 5%.

To optimize experimental conditions, NIST performed preliminary studies with a custom-built 3D printing system. This setup allowed NIST to evaluate sampling port location, flow rate and sampling device impact on particle release rates and sampling efficiency. Commonly used methods for air particle collection include filter sampling, impactor sampling and precipitator sampling. In this preliminary work, NIST compared filter and precipitator sampling and determined that electrostatic precipitator sampling on silicon wafer substrates was the more effective approach. Sampling time was evaluated and NIST noted that sampling for 30 minutes resulted in increased particle concentrations without causing overlapping particles that could interfere with SEM imaging or particle analysis. Both filament types released particles during printing with comparable sizes less than 10 µm and in a wide variety of shapes. Severe charging artifacts² were observed for the neat ABS filament.

NIST designed a full factorial analysis for the two purchased 3D printers. This type of analysis assessed every combination of the five selected variables (printer model, filament type, sampling distance from the printer head, printing temperature and filament storage humidity state). In addition, NIST randomized the order of the experiments to remove any systematic changes such as time of day or building HVAC conditions might play. Two distances from the printer head were compared (25mm and 150mm) as well as two printing temperatures (240°C and 260°C). Printing temperature is one printing parameter that users routinely adjust and can lead to differences in print quality and release rate. Humidity was evaluated by storing filaments in a desiccator or the open lab.

NIST custom built two exposure chambers, one for each 3D printer. NIST also custom built structures to hold the sampling port at the selected studied distances from the printer nozzle due to the different designs of the 3D printers in order to maintain a constant distance as the printer nozzle moved.

NIST used MAPS imaging software to analyze the 100,000 SEM images generated for particle size distribution and number density. Controlled measures were performed to minimize systematic bias in sample imaging. Of the 100,000 SEM images, 800 were selected for manual examination. No individual MWCNTs were found in these high resolution images. Particle dimensions ranged

² Charging effects occur when the sample accumulates electric charge due to the bombardment of the SEM electron beam, resulting in blurring and horizontal streaking and an inability to characterize particles in the affected images.

from a few micrometers to tens of micrometers, with diameters as small as 150nm.³ Some particles had smooth surfaces while others rough. Shapes were spherical to elongated irregular shaped. NIST noted that the smooth surface and rounded shapes were particles formed as the molten ABS droplets solidified. In addition, embedded MWCNTs were observed along with occasional protruding MWCNTs. The rough and irregularly shaped particles were typically larger than the smooth particles. These rough particles were covered with protruding MWCNTs and also contained numerous embedded MWCNTs. The presence of MWCNTs mitigated the charging problem seen with the neat ABS particle samples. Overall, particle size distributions did not differ demonstrably amongst the experimental factors. Higher total particle counts were associated with the open frame printer, printing with neat ABS filaments and printing at the higher extrusion temperature.

NIST concluded that the distance between the extrusion nozzle and the sampling port had the greatest effect on total particle counts sampled. There was an optimal sampling distance of 25mm. The NIST preliminary experiments demonstrated that sampling within a few mm of the extrusion nozzle was not as efficient as the 25mm distance. The influence of other factors on total particle counts was also noted for printer model and filament type (the neat ABS filament produced more particles of respirable size than the MWCNT filament). No free MWCNT particles were detected in the collected samples. MWCNTs were observed embedded and protruding from larger particles.

³ NIST focused only on the respirable fraction of particles (diameters < 10µm) in their analysis. NIST noted in their report that there were few very large particles.

Characterization methods for nanomaterial release during a 3D printing process

Report to the U.S. Consumer Product Safety Commission
Interagency Agreement # CPSC-I-15-0017
ROA #: 643-07-18

Report Date: January 2018

Performed by:

Keana Scott
Samuel Norris
Justin M. Gorham

Submitted by:

Keana Scott^a and Justin Gorham^b
a) Microscopy and Microanalysis Research Group
b) Nanomaterials Research Group

National Institute of Standards and Technology
100 Bureau Drive, MS-8372
Gaithersburg, MD 20877
(301) 975-4579
keana.scott@nist.gov

Disclaimer: Certain commercial equipment, instruments, or materials are identified in this report to foster understanding. Such identification does not imply recommendation or endorsement by NIST, nor does it imply that the materials or equipment identified are necessarily the best available for the purpose.

Table of Contents

| | | |
|-------|---|----|
| 1 | Executive Summary..... | 4 |
| 2 | Introduction | 5 |
| 3 | Survey of consumer 3D printer market | 7 |
| 3.1 | 3D printer selection | 7 |
| 3.2 | 3D printing filaments | 8 |
| 3.3 | Characterization of ABS filaments | 9 |
| 3.3.1 | Fourier transform infrared (FTIR) analysis of filaments | 9 |
| 3.3.2 | Scanning electron microscopy (SEM) analysis of filaments..... | 9 |
| 3.3.3 | Thermal gravimetric analysis (TGA) of filaments..... | 10 |
| 4 | Preliminary Study..... | 10 |
| 4.1 | Standalone printer | 10 |
| 4.2 | Determination of sampling method | 11 |
| 4.2.1 | Filter sampling with polycarbonate (PC) filters: | 12 |
| 4.2.2 | Electrostatic precipitation based sampling..... | 15 |
| 4.3 | Evaluation of released materials using the standalone printer. | 17 |
| 4.3.1 | Results of preliminary testing | 17 |
| 5 | Experimental Design | 19 |
| 5.1 | Experimental factors for printing..... | 19 |
| 5.2 | Statistical sampling | 21 |
| 6 | Testing Apparatus & Procedures | 22 |
| 6.1 | Sampling chambers..... | 22 |
| 6.2 | Sampling setup..... | 23 |
| 6.3 | 3D test object..... | 24 |
| 6.4 | 3D printing procedure..... | 25 |
| 7 | Scanning Electron Microscopy (SEM) | 26 |
| 7.1 | SEM Imaging | 26 |
| 7.2 | Large area tile imaging..... | 26 |
| 7.3 | High resolution imaging..... | 27 |
| 8 | Image Analysis..... | 28 |

| | | |
|-----|--|----|
| 8.1 | Automated image processing | 28 |
| 8.2 | High resolution image analysis | 30 |
| 9 | Results and Discussion | 30 |
| 9.1 | High resolution imaging results | 30 |
| 9.2 | Manual imaging results..... | 35 |
| 9.3 | Automated image analysis results | 38 |
| 10 | Conclusions | 47 |
| | Acknowledgement | 50 |
| | Abbreviations & Terms | 50 |
| | References | 52 |
| | Appendix 1: FTIR spectra of ABS filaments..... | 54 |
| | Appendix 2: MWCNT nanocomposite images | 55 |
| | Appendix 3: Fractional factorial design matrix for single replicate..... | 56 |
| | Appendix 4: 3D Printer chamber cleaning protocol | 57 |
| | Appendix 6: Randomized wafer imaging order | 59 |
| | Appendix 7: FIJI scripts..... | 60 |
| | MAPSPro.ijm | 60 |
| | MAPSPro-bin.ijm..... | 62 |

1 EXECUTIVE SUMMARY

We developed methods to analyze and detect the presence of engineered nanomaterials, specifically multiwalled carbon nanotubes (MWCNTs), in the 3D printing materials and to assess the potential for MWCNT release during 3D printing processes. Thermoplastic 3D printing materials, specifically acrylonitrile butadiene styrene (ABS) in filament form, containing MWCNTs were evaluated by electron microscopy and compared with neat ABS filaments. To assess the potential for MWCNT release, we performed a five factor, two level fractional factorial experiment to determine what experimental variables influence the overall particle release behavior during the 3D printing process. To this end, we fabricated two 3D printing chambers and used them to sample particles released during 3D printing using two different 3D printers. The five factors assessed were as follows: 1) 3D printer model (one per chamber), 2) 3D printing filament type (neat polymer vs. MWCNT nanocomposite polymer) 3) sampling distance from printer head (25 mm vs. 150 mm), 4) printing temperature (240 °C vs. 260 °C), and 5) filament storage condition (in a desiccator vs. exposed to open laboratory humidity).

Air sampling of particles released during 3D printing of a test object was performed at different combinations of experimental factor settings according to the experimental design in a randomized run order. Particles collected onto silicon wafers using an electrostatic precipitator were imaged using a scanning electron microscope (SEM) to assess for number of released particles in the respirable size range (<10 µm) and to screen for individual MWCNT release.

The following are the main conclusions from this study:

- Sampling location has the greatest effect on the total particle counts. In general, sampling closer to the particle source resulted in higher total particle counts. Sampling closer than 25 mm however, resulted in inefficient particle collection.
- Neat ABS filament produces more particles of respirable size than MWCNT ABS filament during 3D printing.
- Printing temperature ranges tested in this study had the lowest impact on total particle counts.
- All experimental conditions produced similar particle distribution with a single major peak around 300 nm. There were several conditions where a smaller secondary peak was seen at 500 nm or 700 nm in the form of a shoulder. Although 4 out of 5 instances, the secondary peak was detected when neat ABS filament was used, there was no simple relationship between the appearance of the secondary peak and the main experimental factors.
- Humidity effects were difficult to determine because of the confounding of factors due to blocking used in our fractional factorial design.

- Most of the particles sampled were less than 2 μm in diameter. It should be noted that the range of sampled particle sizes depends on the sampling method and should not be confused with the range of released particle size.
- Many of the particles sampled during the MWCNT ABS filament printing were found to contain MWCNTs. Some particles had smooth surfaces and most MWCNTs were embedded within the particles. Some particles had irregular morphologies with protruding MWCNTs covering the particle surface.
- Most of the particles containing MWCNTs were greater than 2 μm in diameter.

Although we were able to identify a couple of main factors that affect the total particle counts, large discrepancies between replicates and confounding effects made it difficult to assess more nuanced interaction effects between factors. For the next phase of this study, we will need to reduce the measurement uncertainty by increasing the replicate to replicate consistency. We also need to determine the relationship between particles released and particles sampled with respect to concentration and size range to understand hazards associated with the 3D printing process. This will require a control MWCNT aerosol source which is well-defined and uniformly dispersed. Although there are many methods for testing particle sampling efficiency using polymer beads or other spherical particles, currently we do not have a method to consistently disperse MWCNTs and use it to characterize the performance of different sampling methods. Our next effort will focus on developing a method to generate robust and well characterized MWCNT control dispersion.

2 INTRODUCTION

The National Institute of Standards and Technology (NIST) has been tasked by the U.S. Consumer Product Safety Commission (CPSC) to develop test and analysis methods for detecting the presence of multi-walled carbon nanotubes (MWCNTs) in consumer grade 3D printing materials and assessing the release of MWCNTs during the printing process, in accordance with Interagency Agreement # CPSC-I-15-0017. Although the current report focuses on detection of MWCNT during 3D printing using polymer composites containing MWCNTs, the methods discussed in this report can be used for other types of polymer nanocomposites used in additive manufacturing.

3D printing is a type of additive manufacturing that makes use of printing technologies to create three dimensional objects using a layer-by-layer approach from raw composite filaments and a digital model. While 3D printing technology has been developing over the past few decades as a tool for industrial scale manufacturing, in the past 10 years the technology has become more cost effective and user friendly, resulting in an increase of units purchased for personal use [1]. Since 2007, when the first 3D printing systems under \$10,000 became

available, the number of 3D printer models commercially available has been growing rapidly. When this project was initially proposed in the fall of 2015, there were 235 different 3D printer models available according to 3D Hubs website (<https://www.3dhubs.com>, accessed September 28, 2015). This number grew rapidly to 441 by December 1, 2015 and to 668 as of January 2, 2018. Similarly, the total 3D printer sales number grew rapidly since 2007, as shown in Figure 1. Today, 3D printers are widely available at schools, libraries, and offices as well as in homes.

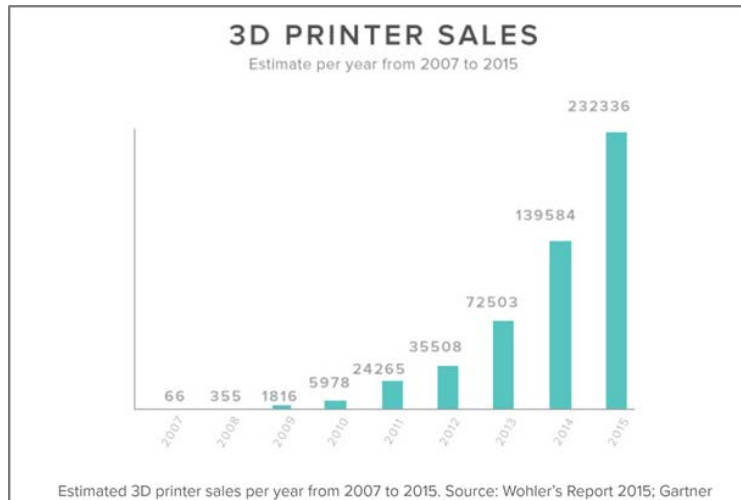


Figure 1: Estimated 3D printer sales per year from 2007 to 2015. <https://www.3dhubs.com/what-is-3d-printing> (accessed January 1, 2018)

Although there are several different printing technologies available, most of the affordable consumer grade 3D printers make use of technology called fused filament fabrication (FFF) where a thermoplastic polymer filament (*e.g.* acrylonitrile butadiene styrene (ABS), polylactic acid (PLA), Nylon, etc.) is used as the feedstock material to make items during the printing process. This filament can be a neat polymer or a composite with one or more non-polymer fillers such as metal powders, clay, wood fibers, and engineered nanomaterials to lend the printed object desirable material properties.

A nanomaterial is defined as a material that ranges in size from 1 nm to 100 nm in at least one dimension [2]. Some examples of nanomaterial fillers used as filaments for 3D printing include carbon nanotubes, carbon fibers, and metal/metal oxide powders [3,4]. Much of the reason for incorporating MWCNTs into a 3D printer filament or any other composite is to lend the material enhanced properties such as mechanical strength or conductivity. While these nanocomposite filaments can then be used to create 3D printed items with enhanced physical properties, the potential may exist for nanomaterials to be released during the printing process, leading to nanomaterial accumulation in the surrounding environment (*e.g.* settled particulates and dusts in indoor public space or home workshop) and individuals' exposure to released nanomaterial during printing processes (*e.g.* inhalation). Due to their potential for health

hazards, it is important to determine whether the MWCNTs are being released during printing and, if released, in what form (*e.g.* composite particle vs. free tubes) the nanomaterials are released [5].

The purpose of the work under this agreement is to develop analytical techniques and assess the presence of engineered nanomaterials, specifically MWCNTs, in the 3D printing materials and the potential for MWCNT release during 3D printing processes.

3 SURVEY OF CONSUMER 3D PRINTER MARKET

3.1 3D printer selection

3D printers were evaluated based on freely available market report sites such as 3D Hubs (<https://www.3dhubs.com/>) and PC Magazine (<https://www.pcmag.com>) that rate products based on metrics such as ease of use, print quality, and cost. Most cost-effective 3D printers used by hobbyists and small businesses are based on an FFF process which operates by printing molten polymeric filaments in a layer-by-layer approach following a computer-generated model. Other 3D printing technologies such as vat photopolymerization, powder bed fusion, material jetting, and direct energy deposition can produce objects with more complex shapes and better material properties than FFF. However, most of the non-FFF technology-based printers are still too expensive for general purpose Do-It-Yourself (DIY) 3D printing. For this study, we selected two 3D printers based on the following criteria: 1) affordability while maintaining versatility in consumer application, 2) broad utilization across the 3D printing community, and 3) moderate (middle-of-the-road) performance rating with respect to ease of use and failure rate. The first two criteria were an obvious attempt at maximizing the impact and relevance of the model chosen. Moderate ratings, instead of best ratings, for ease of use and failure rate were chosen as a qualification for 3D printers since these models would more likely reflect sources of potential failure as compared to their relatively flawless counterparts.

The first of the two printers was the Printer 1 which is an enclosed system with a heated, static build plate, as shown in Figure 2 (left). Printer 1 model was one of the first consumer level 3D printers that became very popular. Although more advanced and comparably priced 3D printers are now on the market, Printer 1 3D printers are common printers one encounters at schools, libraries, and small business settings.



Figure 2: (left) Printer 1 and (right) Printer 2

To maximize the differences in configuration, we selected Printer 2 as our second 3D printer. Printer 2 is an open frame printer with a mobile heated platform while Printer 1 is a partially enclosed printer with a stationary heated platform. We hypothesized that an open frame printer was likely to have a larger direct user exposure than an enclosed system with respect to aerosolized particles being released. The selection of these two printers allowed us to evaluate two extreme scenarios.

3.2 3D printing filaments

3D printing filaments can be made from a number of different thermoplastics, including variants in polymers such as PLA, ABS, polyethylene terephthalate glycol (PETG), and high impact polystyrene (HIPS). Although many different types of 3D printer filaments are commercially available and custom mixture of fillers and polymers can easily be fabricated using consumer grade materials and equipment, currently Manufacturer 1 is the only manufacturer we are aware of that sells MWCNT nanocomposite filaments. In 2015, when we were initially surveying the MWCNT nanocomposite filament market, Manufacturer 1 only sold PETG, PLA and ABS nanocomposite filaments. We decided that ABS nanocomposite filaments are more promising 3D printing material for structural and electronic components and other general-purpose 3D printed objects due to their strength and thermal stability compared to PLA or PETG. For this project, we chose a MWCNT ABS composite filament from Manufacturer 1 (see Figure 3). Additionally, a neat ABS filament was purchased from Manufacturer 1 to have a direct comparison of the same material from the same manufacturer. It is important to note that the concentration of MWCNTs in the Manufacturer 1 filaments was unknown, presumably due to proprietary information claims from the manufacturer. From here on, we will use the terms ‘MWCNT ABS filament’ and ‘neat ABS filament’ for Manufacturer 1 ABS filament and Manufacturer 1 Natural ABS filament, respectively.



Figure 3: Images of the different filaments used in this study: MWCNT ABS (left) and neat ABS (right).

3.3 Characterization of ABS filaments

3.3.1 Fourier transform infrared (FTIR) analysis of filaments

Small pieces of the neat ABS and MWCNT ABS filaments were analyzed using a Smiths IlluminatIR™ FTIR system in the attenuated total reflection (ATR) mode. ATR spectra of the neat ABS and MWCNT ABS filaments confirmed that the matrix polymer as ABS. A neat ABS filament sample from another manufacturer was also analyzed and found to have the absorption bands characteristic of ABS [6]. See Appendix 1 for the ATR spectra of the filaments.

3.3.2 Scanning electron microscopy (SEM) analysis of filaments

A fragment of MWCNT ABS filament was mounted on an aluminum pin stub using a double-sided carbon tape and examined in an SEM. The exposed cross-sectional surface of the filament showed numerous protruding and embedded MWCNTs (Figure 4a and b), confirming the presence of MWCNTs in the filament. Bright thread like feature in Figure 4a and spaghetti like bundles in Figure 4b are MWCNTs. In contrast, Figure 4c presents the cross-sectional face of neat ABS filament, revealing a surface free of MWCNTs; note however this image exhibits severe charging artifacts.

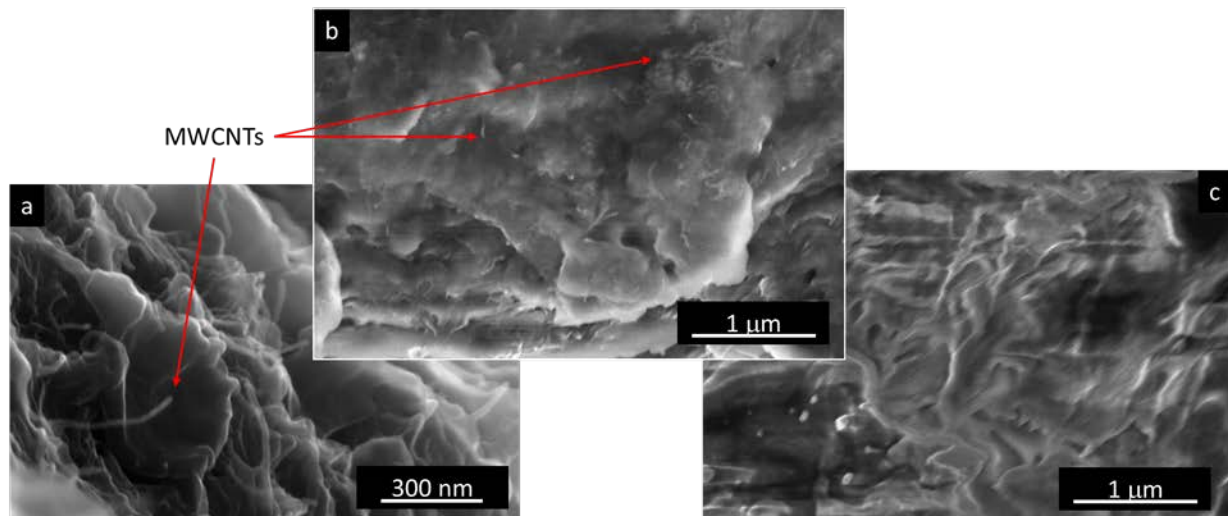


Figure 4: SEM images of MWCNT ABS (a & b) and neat ABS (c) filament fragment surfaces. MWCNT ABS filament cross-section surfaces show many protruding and embedded MWCNTs (red arrows) while neat ABS filament fragments do not show corresponding features and exhibit severe charging artifacts (blurring of the image).

3.3.3 Thermal gravimetric analysis (TGA) of filaments

TGA was also performed on the MWCNT and neat ABS filaments to determine the rough estimate of the mass fraction of MWCNTs in the nanocomposite ABS filament. Data acquisition was carried out using a TA Instruments TGA Q500. MWCNT ABS and neat ABS filament samples were run under N₂ condition at a heating rate of 5 °C/min from room temperature to 650 °C. The mass fraction of MWCNTs in MWCNT ABS filament was determined by taking the residual mass fraction at 500 °C for MWCNT ABS filament and subtracting the residual mass fraction at 500 °C for neat ABS filament. All specimens were measured in triplicate, with initial sample masses ranging from 8.86 mg to 9.95 mg. The estimated mass fraction of MWCNT in the MWCNT ABS filament is ≈5 %. Table 1 summarizes the TGA results.

| Replicate | Neat ABS | | MWCNT ABS | | Δ mass fraction (%) |
|-----------|-----------|-------------------|-----------|-------------------|---------------------|
| | temp (°C) | mass fraction (%) | temp (°C) | mass fraction (%) | |
| 1 | 499.99 | 2.26 | 499.98 | 7.40 | |
| 2 | 499.99 | 2.53 | 500.02 | 7.39 | |
| 3 | 500.00 | 2.25 | 500.00 | 7.48 | |
| Average | | 2.35 ± 0.13 | | 7.42 ± 0.04 | 5.07 ± 0.17 |

Table 1: Mass fraction (%) remaining of all samples and Δ mass fraction (%) of the average neat ABS and average MWCNT ABS under nitrogen.

4 PRELIMINARY STUDY

To assess particle release from the 3D printing process, two main points had to be considered: 1) pertinent experimental factors for 3D printing operation; and 2) sampling method for collecting released particles during 3D printing. During the preliminary study, a series of exploratory experiments were performed towards determining optimal experimental configurations and procedures.

4.1 Standalone printer

Effective 3D printing, in practice, requires the use of proper printing parameters including extruder temperature, filament feed rate, filament diameter, and filament condition. One of the key questions was: *which of the 3D printing parameters has a significant impact on the release rate?* To answer this question, first we needed to determine the limits of 3D printing parameter space - a set of operational ranges for the basic 3D printing parameters. To this end, we fabricated a standalone 3D printer consisting of a print head (filament feeder, heater, and extrusion nozzle) and the control software for the print head (See figure 5). An adjustable sampling port was included to measure release of particulates and to explore how parameters such as sampling port location, flow rate, and sampling device impact both release rate and sampling efficiency.

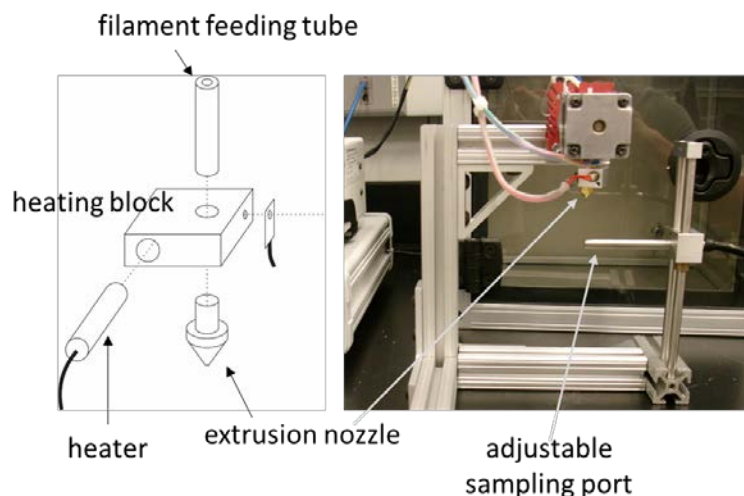


Figure 5: (Left) Diagram of the heating block, extruder and temperature control system for the standalone 3D printer. (Right) Image of the fully assembled standalone 3D printer.

The basic standalone 3D printer was assembled from commercially available parts such as a Spitfire Extruder (Deezmaker), a stepper motor (Kysan Electronics) and controller (Phidgets), and temperature control components (Omega). The extruder assembly was mounted on a stationary aluminum scaffold (80/20) with a built-in, adjustable mount for a stainless steel tube near the extrusion nozzle. The stainless steel tube acted as the sampling port through which particles emitted during extrusion can be collected, using a sampling device such as a filter sampler or electrostatic precipitator, on to a substrate. Subsequent SEM analysis of the particles captured on the substrate during extrusion was used to assess the effectiveness of the printing and sampling parameters. A custom LabVIEW (National Instruments) graphical user interface (GUI) was used to control the settings on the standalone 3D printer system.

4.2 Determination of sampling method

A key component of this study is the collection of released particles from air around the printing device during 3D printing. Commonly used approaches for air sampling of particles are filter sampling, impactor sampling, and precipitator sampling. Our earlier work on the evaluation of release particles using micro-orifice uniform deposit impactor (MOUDI) sampling showed that the analysis requirements for MOUDI substrates are too labor intensive for nanoparticle detection and analysis because each MOUDI run generates multiple samples that must be analyzed [7]. For the current study, we only considered filter sampling and precipitator sampling approaches. Filter sampling was performed using track-etched polycarbonate membrane filters in single-use filter housing. For precipitator sampling, an electrostatic precipitator was used to deposit particles on a silicon wafer substrate. Ultimately, the electrostatic precipitator sampling was deemed a more effective approach. Details of the

operating conditions and sampling setup for the electrostatic precipitator are described in the following section.

4.2.1 Filter sampling with polycarbonate (PC) filters:

Filter sampling was performed using track-etched polycarbonate membrane filters (Whatman, Nuclepore Track-Etched Membranes, 25 mm diameter) in Asbestos style conductive air sampling cassettes (25 mm, Zefon International). Figure 6 shows a photo and a schematic diagram of a sampling cassette. A membrane filter is held in place by a support pad above the cowl. Several different flow rates, filter pore sizes, and filter types were tested to determine the optimal sampling configuration.

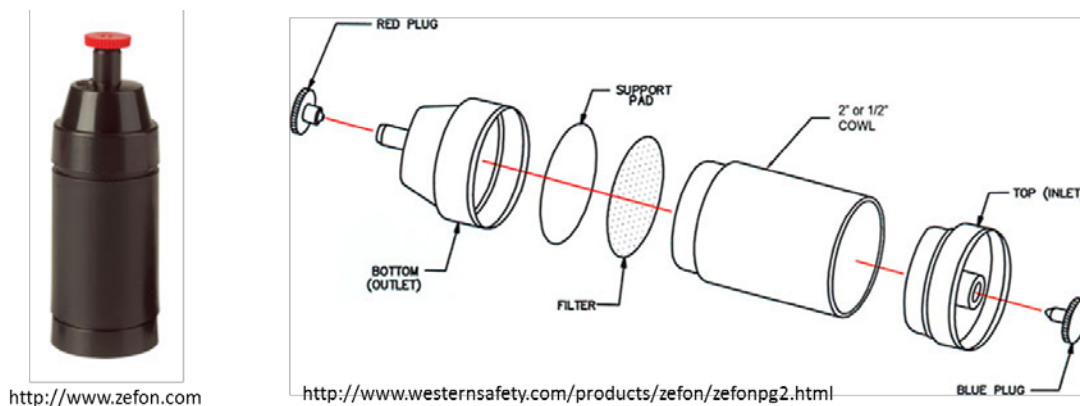


Figure 6: Photograph and schematic diagram of a conductive air sampling cassette. A membrane filter is placed in the cassette using a filter support pad.

Many of the personal samplers used for health monitoring require relatively low flow rates (typically 3 L/min or less) while large volume monitoring methods such as MOUDI require higher flow rates (15 L/min and higher). Using the standalone 3D printer system described earlier, we tested several different filter pore sizes ranging from 0.03 μm to 0.8 μm and decided on the 0.4 μm pore size filters for further testing. Smaller pore size filters required flow rates well below 3 L/min for a stable setup and, consequently, an extended sampling period (over 30 minutes) for any detectable particle accumulation. Additionally, for aerosol sampling, filter pore size does not represent the smallest particle size one can collect. For liquid filtration, interception (capturing of particles that are larger than the filter pore diameter) is the main factor in collection efficiency. However, for aerosol sampling, Brownian diffusion, inertial impaction, and gravitational settling also contribute to the total particle collection efficiency in addition to interception [8]. Because of this, particles much smaller than the pore diameter can be collected even if we are using a 0.4 μm pore size membrane filters.

We also tested two different types of track etched polycarbonate (PC) membrane filters: uncoated PC membrane filters and gold coated PC membrane filters. Uncoated filters were more cost effective than the gold coated filters but required additional conductive coating to mitigate sample charging during SEM imaging. Also, uncoated membrane filters were extremely flimsy and, thus, easily creased or damaged during handling and very difficult to lay flat on SEM sample holders. We rely on the automated SEM imaging software to image a relatively large area of each filter for statistically significant sampling. Because autofocusing routine can take several minutes to run, for large area automated imaging (or tile imaging) runs, it is necessary to have a very flat sample surface to avoid the need to autofocus prior to collecting each tile image. With uncoated membrane filters, it was difficult to acquire useful SEM images without frequent focus adjustments.

Although gold coated filters were easier to handle than the uncoated filters and had the advantage of mitigating charging artifacts during SEM imaging, the coated filters showed uneven surface texture (surface undulation seen in the center image of Figure 7) that made automated imaging challenging. Also, the fine-scale mottling in contrast as shown in the inset images of Figure 7 was frequently segmented as particles during automatic thresholding processes, making automated particle detection challenging.

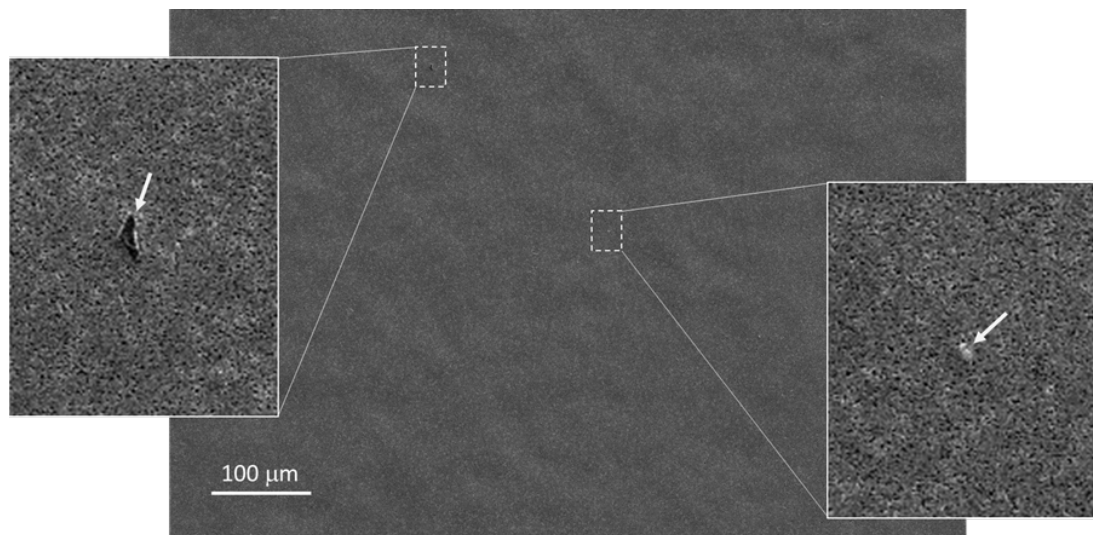


Figure 7: Low resolution overview image of a gold coated PC membrane filter after a sampling run. Inset images show magnified images of the particles (indicated by white arrows) found on the filter.

We were able to collect particles with wide ranges of size (few nm to few tens of μm) and shape (spheres, platelets, agglomerates, etc.) on both the uncoated and the gold coated filters during the sampling tests. Figure 8 shows several examples of these particles. Figure 8a) shows an agglomerate of polymer fragments and MWCNTs that might have been broken apart upon impacting the filter surface. In addition to the larger agglomerate, smaller agglomerates and

nanometer sized individual particles are also present. Figures 8b and c show smaller agglomerates of polymer fragments and MWCNTs. Figure 8d) shows a portion of a larger particle where numerous MWCNTs are protruding from the particle surface. Figure 8e) shows a larger particle with an irregular shape. Although the particles shown in Figure 8 all contain MWCNTs, we also found numerous polymer particles and fragments without MWCNTs. However, high resolution imaging of these particles was not attempted because of severe charging artifacts.

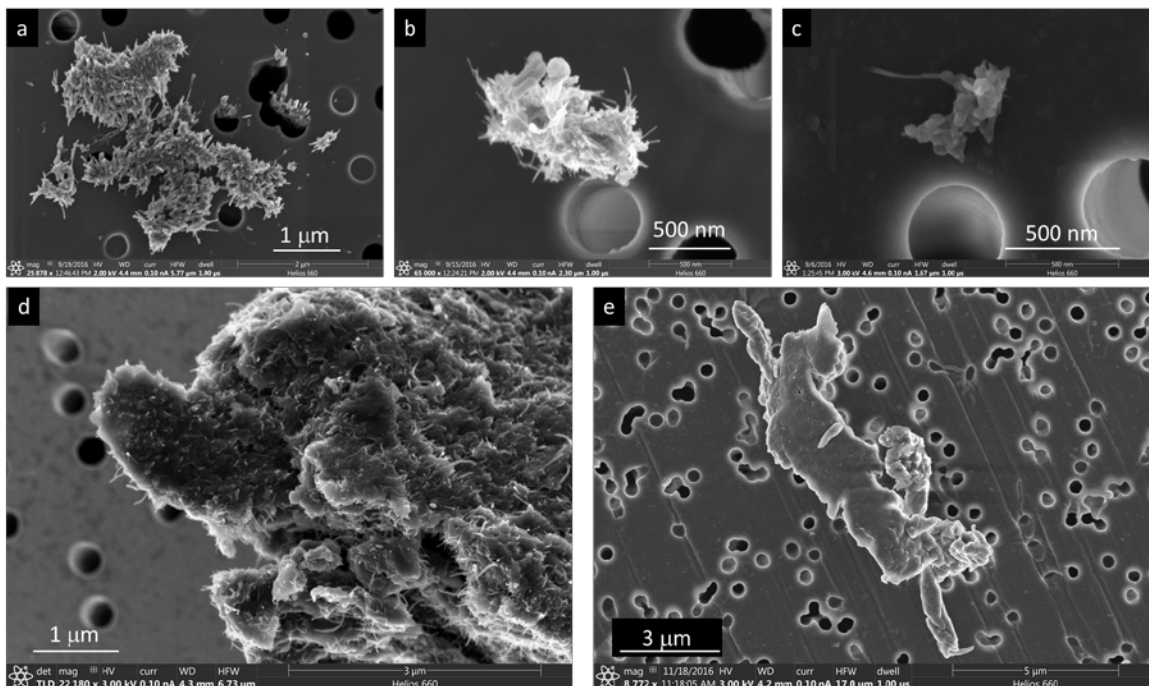


Figure 8: SEM images of particles collected on the membrane filters showing different sizes and shapes of the particles. Panels a, b, c, & e are from uncoated membrane filters and panel d is a particle from gold coated membrane filter.

The biggest challenge in using filter sampling for nanoparticle detection is the difficulty in correctly segmenting captured particles, and nothing else. Figure 9 effectively illustrates this problem. Figure 9a is an SEM image of a small particle on a membrane filter surface. The numerous small circular features with similar contrast as the particle are the track-etched pores. Due to a phenomenon called edge effect, filter pores appear as bright rings in the image. The basic idea behind edge effect is that additional secondary electron signal is produced at the edges of an object (in our case edges of the pores) being imaged, making the feature appear brighter in an SEM image [9]. Because of this, the pores have the similar intensity level as the particle in the center of the image and there is no easy way to differentiate the particle from pores in an automated manner. Figure 9b shows a binary image generated from the SEM image by applying a thresholding operation. Most of the pores are

still visible and correct segmentation of the particle can only be achieved with manual intervention.

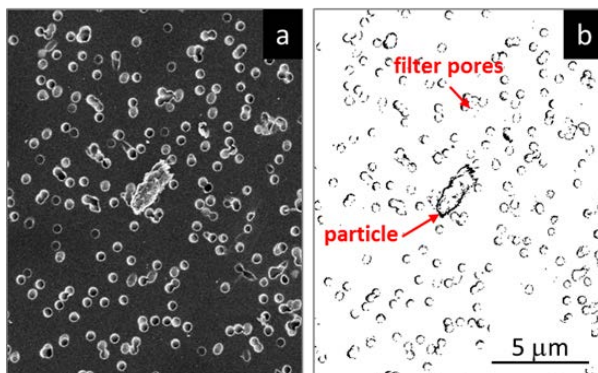


Figure 9: a) SEM image of a typical filter surface with a captured particle and b) the binary image of the same.

4.2.2 Electrostatic precipitation based sampling

A TSI Nanometer Aerosol Sampler (NAS) Model 3089 (TSI, Shoreview, MN) was used to sample the air near the printing head during the 3D printing operations. NAS is an electrostatic precipitator where the charge applied to the sampling substrate helps preferential collection of opposite charge particles entrained in the inlet air stream (see Figure 10). NAS can also be run at neutral charge. For this work, we used 25 mm polished silicon wafers (Virginia Semiconductor, VA) as the collection substrate. NAS was operated at various voltages ranging from 0 kV (neutral) to -10 kV and the resulting Si substrates were analyzed for maximum particle collection efficiency.

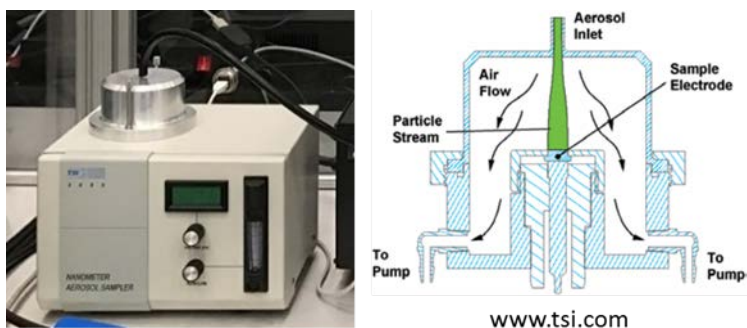


Figure 10: Photograph and the schematic diagram of a Nanometer Aerosol Sampler (NAS).

Several different sampling durations ranging from 3 min to 30 min were tested to assess the particle loading on silicon wafers and appropriate SEM imaging conditions. Silicon wafers from these runs were, then, analyzed in an SEM using an automated large area imaging routine. Details of the SEM imaging procedures are described in Section 7. A sufficiently large area of each silicon wafer was imaged to assess the overall particle distribution pattern and particle number density. Figure 11 shows the stitched tile images from a 3 min run and a 30 min run. In both images, particles tend to concentrate in the center of the wafer where the aerosol inlet of

the NAS was directed and particle concentration diminished with increasing radial location. We found that the 3 min sampling run resulted in a very low surface concentration of particles. Increasing the sampling time to 30 minutes resulted in increased particle concentrations without causing overlapping particles that can interfere with SEM imaging or particle analysis.

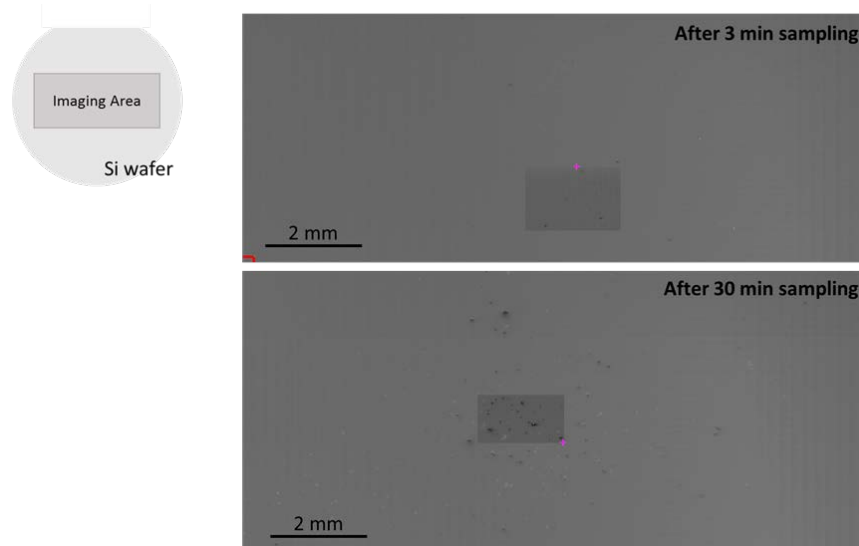


Figure 11: Stitched SEM tile images from two different duration NAS sampling runs showing differences in the number of particles collected over 3 min (top) and 30 min (bottom) sampling runs. Two rectangular regions correspond to the ‘imaging area’ shown on the silicon wafer diagram (left).

Based on our preliminary test results, we decided on the NAS (electrostatic precipitator) sampling of particles onto 25 mm silicon wafer as our sampling strategy. We decided against the filter sampling mainly based on the difficulty of analyzing the particles on the membrane filters. Table 2 summarizes the pros and cons of the two sampling methods considered.

| Sampling Method | Substrate | Notes |
|---|-------------------------|--|
| Membrane filters in air sampling cassette | Uncoated 400 nm pore | Good collection efficiency but difficult to handle and requires conductive coating for imaging |
| | Uncoated 30 nm pore | Requires low flow rate sampling. Low collection efficiency. |
| | Gold coated 400 nm pore | Good collection efficiency, good conductivity (does not require coating) Uneven surface and mottling in contrast (difficult for image processing) |
| NAS | Si wafer | Good collection efficiency and good conductivity. Easy to handle. -8 kV NAS voltage collects most particles. |

Table 2: Summary of the sampling methods

4.3 Evaluation of released materials using the standalone printer.

Once the operational ranges of various 3D printing and sampling parameters were determined, we proceeded to confirm that our sampling and analysis approach can detect the release of particulates during 3D printing processes. To accomplish this, both the neat and the MWCNT ABS filaments were extruded using the standalone printer described in Section 4.1. After testing several different locations, a sampling port location proximate to the extrusion nozzle, as shown in Figure 5 (right), was used for the initial sampling tests. NAS sampling was used to deposit particulates on to silicon wafers that were analyzed using SEM to confirm particle release. While not explicitly detailed below, additional variables such as extruder temperature and extrusion rate were also evaluated. Results from these tests helped instruct our choices in variables to examine in the subsequent and more comprehensive study.

4.3.1 Results of preliminary testing

Using the standalone 3D printing setup, we evaluated the basic 3D printing configurations and the feasibility of our release particle sampling configurations using both neat and MWCNT ABS filaments. Figure 12 and Figure 13 show select SEM images from the 3D printing tests using the standalone printer with neat ABS and MWCNT ABS filaments, respectively. For both filaments, there was clear evidence of release in the form of particulates. Images from the neat ABS filaments (Figure 12) show that the particles are typically less than 10 micrometers in size and have a wide variety of shapes and sizes. Although SEM imaging was performed using a low electron beam accelerating voltage (3 kV) and low current (100 pA), larger particles exhibited severe charging artifacts, as expected from non-conducting polymer particles. For example, the horizontal streaking seen in Figures 12d and e and blurring of some of the features in Figures 12a, b, and d are due to charging. In general, smaller particles such as shown in Figures 12a, b, and c are more angular in shape while larger particles tend to have elongated and irregular shapes with heavily wrinkled surfaces similar to those seen in melted and re-solidified surfaces.

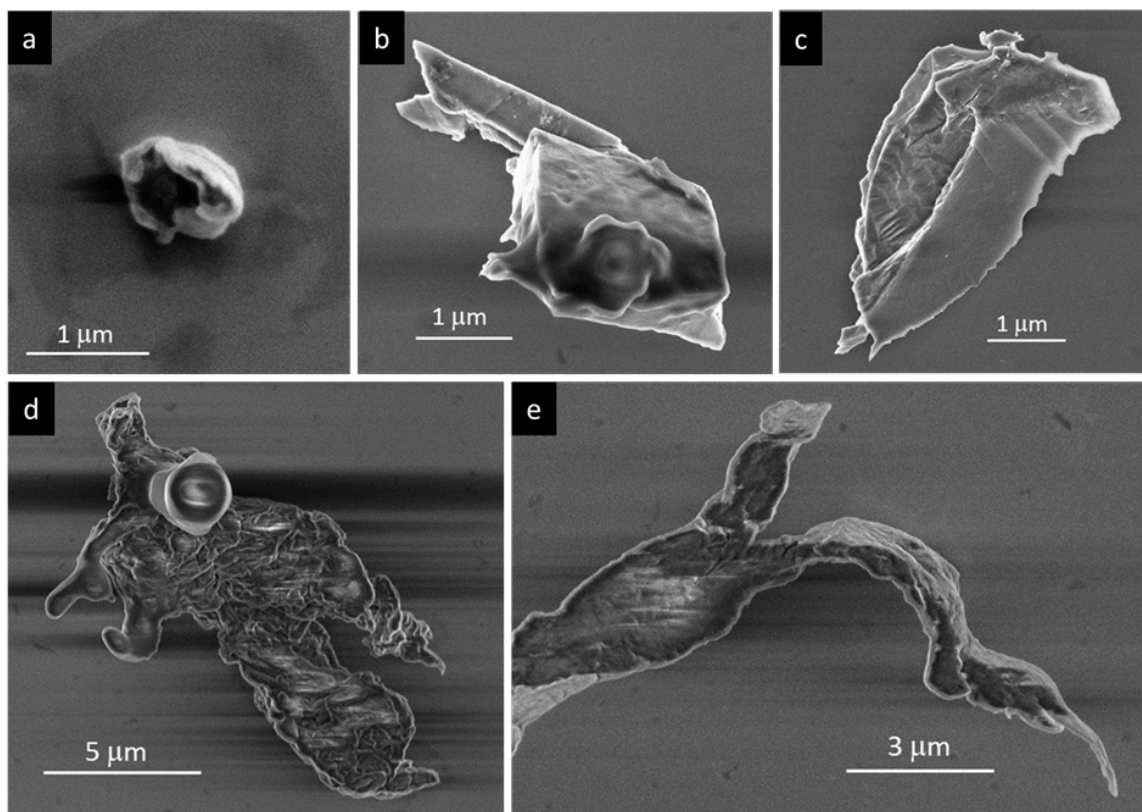


Figure 12: SEM imaging of released particulates from the standalone 3D printer using the neat ABS filaments.

The size of the released particles observed for the MWCNT ABS filaments during 3D printing were comparable to their neat ABS filament counterparts. Some of the smaller particles showed angular morphology similar to those from the neat filament tests (Figure 13d) and many of the larger particles had elongated and ribbon like shapes (Figure 13e). Although the particle morphology was similar to those from the neat ABS filament test, larger elongated particles from the MWCNT ABS filament tests did not exhibit the same level of charging during imaging. High resolution view of the particle surface (Figure 13f) showed fibrous inclusions (indicated with red arrow) all over the particle surface. We have shown in our earlier study that these tangled fibrous inclusions are buried MWCNTs [10]. See Appendix 2 for example images. We also saw several irregularly shaped platy particles (Figure 13a). Upon closer inspection, these particles usually showed very uneven surface morphology and had numerous fibrous protrusions extending from the particle surface. Figure 13b is a magnified image of Figure 13a inset showing rough particle surface and many protruding fibers. Again, based on our previous experiences, these fibrous protrusions are partially embedded MWCNTs. A crude evaluation of the protrusions in the observed images is consistent with MWCNTs characterized by diameters on the order of 20 nm. In contrast, particles originating from the neat ABS filament did not exhibit any buried MWCNTs or protrusions consistent with MWCNTs.

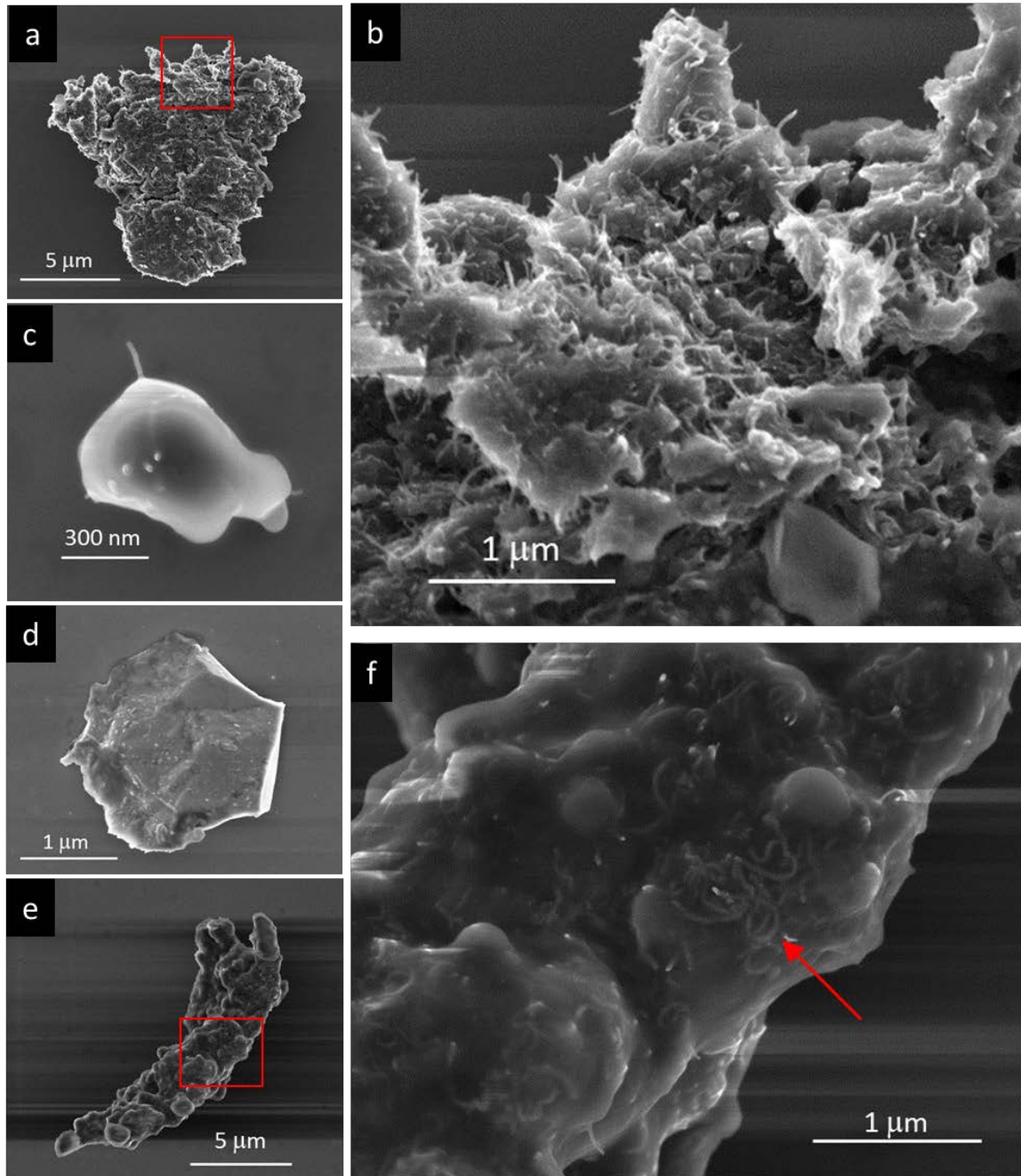


Figure 13: SEM imaging of released particulates from the standalone 3D printer using the MWCNT ABS filaments. Panel (b) is a high resolution image of the inset region (red box) of the irregular platy particle in panel (a). Panel (f) is a high resolution image of the inset region of the elongated particle in panel (e).

5 EXPERIMENTAL DESIGN

5.1 Experimental factors for printing

Following the preliminary study to determine the realistic experimental parameter ranges and sampling approach, a study was designed to evaluate the impact of different printing and

sampling variables, or experimental factors, on release rate and likelihood of individual's exposure to released material in the presence of an operating 3D printer. The two obvious factors, namely the printer model and the printing filament type, were already discussed in Section 3. However, for a given printer and filament combination, there are many other parameters that can impact the particle release behavior during printing. Several additional rounds of sampling tests were conducted using the standalone 3D printer setup to determine the printing and sampling parameters that impacted the number and type of particles collected on silicon wafers. Silicon wafers were, then, analyzed in an SEM to qualitatively assess the collected particle number density. While many different parameters were examined, due to time and resources constraints, we needed to limit the number of experimental factors for our study design.

In the end, total of five factors were chosen for this study. These factors and the different levels assigned for each factor are listed in Table 3. As previously stated, the first two factors were the printer model (X1) and the MWCNT concentration (X2) in the filament. Sampling distance (X3) was the third factor chosen, based on the assumption that direct exposure to airborne particulates is related to the distance from the source. The fourth factor, printing temperature (X4), is one of the printing parameters that are routinely adjusted by users and can easily lead to differences in print quality and release rate. The final factor was filament storage humidity (X5). Previously, we have observed variations in the print quality with filaments left in the open laboratory environment. Since the manufacturer recommends storage of filaments in a desiccator, the two levels chosen were storage in ambient laboratory humidity and in a desiccator. For factors X3, X4 and X5, the 2 levels were chosen to represent the extreme ends of a range reasonably expected to be used in most 3D printing experiments.

| Factor | Level | Assignment |
|-------------------|-------|---|
| X1: Printer Model | - | Printer 1 |
| | + | Printer 2 |
| X2: Filament Type | - | Neat ABS |
| | + | MWCNT ABS composite |
| X3: Distance | - | Near (~2.5 cm) |
| | + | Far (~15 cm) |
| X4: Temperature | - | Low (240 °C) |
| | + | High (250 °C for MakerBot, 260 °C for TAZ5) |
| X5: Humidity | - | Dry Box |
| | + | Lab Humidity |

Table 3: Experimental design factors and level assignments for the 3D printing experiments. – and + represent the two different levels chosen for each factor.

5.2 Statistical sampling

Development of an approach was necessary to both optimize the use of limited time to produce deliverables while maintaining statistical relevance of the results regarding the importance of the variables. It was also necessary to account for the requirement of replication to test the repeatability of these findings. To address repeatability, all experiments were duplicated for direct comparison. Initially, a full factorial analysis, which assesses every possible combination of the 5 variables, was considered. Full factorial analysis with 2 replicates would have resulted in $2^5 \times 2$ experiments (n=64) but this was not feasible in terms of time and resources. We opted for a fractional factorial design with 2 replicates which would reduce the number of experiments to $2^{5-1} \times 2$ (n=32). Ultimately, it was decided to employ a full factorial design for factors X1, X2, X3, and X4, while X5 was confounded with interaction term X3*X4. With 2 replicates, this design gave us 32 possible combinations of experimental conditions. See Appendix 3 for the fractional factorial design matrix for a single replicate. This allowed us to study the effects of instrument model and MWCNT concentration on the release rate, estimate the impact of the sampling location, printing temperature and filament humidity, and verify the repeatability in the time available.

| Config | Printer | Filament | Distance | Temp | Humidity | Replicates | Run Order |
|--------|---------|----------|----------|--------|----------------|------------|-----------|
| C01 | | Neat | Near | 240 °C | Room Condition | 1 & 2 | 11, 28 |
| C02 | | Neat | Near | 250 °C | Dry Box | 1 & 2 | 8, 20 |
| C03 | | Neat | Far | 240 °C | Dry Box | 1 & 2 | 3, 25 |
| C04 | | Neat | Far | 250 °C | Room Condition | 1 & 2 | 10, 21 |
| C05 | | MWCNT | Near | 240 °C | Room Condition | 1 & 2 | 2, 17 |
| C06 | | MWCNT | Near | 250 °C | Dry Box | 1 & 2 | 15, 32 |
| C07 | | MWCNT | Far | 240 °C | Dry Box | 1 & 2 | 14, 24 |
| C08 | | MWCNT | Far | 250 °C | Room Condition | 1 & 2 | 5, 29 |
| C09 | | Neat | Near | 240 °C | Room Condition | 1 & 2 | 6, 18 |
| C10 | | Neat | Near | 260 °C | Dry Box | 1 & 2 | 13, 31 |
| C11 | | Neat | Far | 240 °C | Dry Box | 1 & 2 | 1, 23 |
| C12 | | Neat | Far | 260 °C | Room Condition | 1 & 2 | 16, 30 |
| C13 | | MWCNT | Near | 240 °C | Room Condition | 1 & 2 | 9, 26 |
| C14 | | MWCNT | Near | 260 °C | Dry Box | 1 & 2 | 7, 19 |
| C15 | | MWCNT | Far | 240 °C | Dry Box | 1 & 2 | 12, 27 |
| C16 | | MWCNT | Far | 260 °C | Room Condition | 1 & 2 | 4, 22 |

Table 4: 3D printing fractional factorial experimental conditions and the randomized replicate 1 and replicate 2 run orders for each condition.

Lastly, a randomized order was set for each of the 32 experiments to eliminate any systematic changes such as time of day dependent temperature or air handling condition in the building. The exception was that all of replicate 1 was measured before the start of replicate 2. Table 4 provides the sampling conditions and the order (run order) they were performed.

6 TESTING APPARATUS & PROCEDURES

6.1 Sampling chambers

Two separate enclosure chambers were constructed from extruded aluminum framing and acrylic paneling (80/20 Inc, Columbia City, IN), as shown in Figure 15. Each chamber was 114 cm wide by 127 cm tall by 61 cm deep and housed a 3D printer (Printer 1 or Printer 2). Although rubber gaskets were used to hold the acrylic paneling in the T-slot frames, the chambers were not designed to be air tight. Ports for high efficiency particulate air (HEPA) filtered inlet air were distributed across the back of the chamber. Another port in the front of the chamber was used as the exhaust port for the filtered output from the sampling device. A separate port was dedicated for the electrical cords for the printer and the sampling devices.

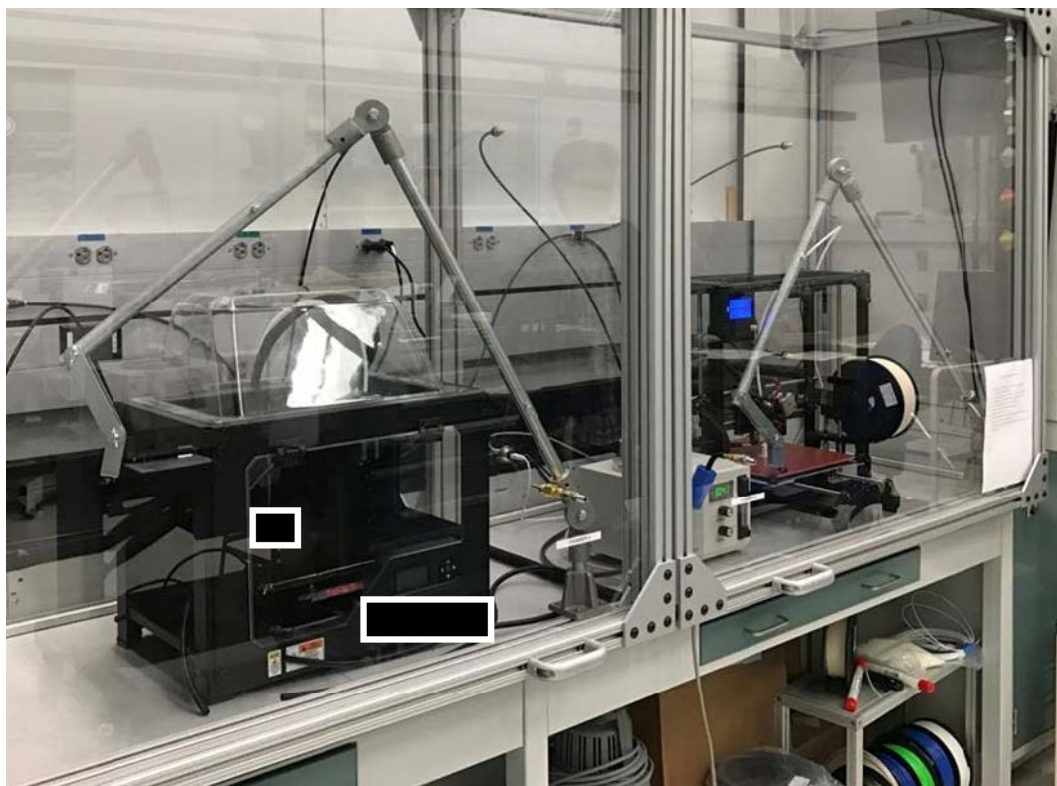


Figure 15: Photograph of the custom-built chambers. Each chamber has sufficient space to house a 3D printer, the NAS device, and the sampling hookups.

6.2 Sampling setup

Sampling setup used in this study is schematically depicted in Figure 16. Here, the outer dashed box represents the sampling chamber. Sampling port was a ≈ 7.6 cm long stainless steel tube attached to a conductive rubber hose (≈ 56 cm in length) which was connected to the NAS (Figure 10) on the other end. The experimental factor X3 was the distance between the sampling port and the printing nozzle, a key variable to consider when evaluating exposure to released particles. The two levels for this factor were *near* and *far* sampling port locations. The *near* level referred to holding the sampling port as close as possible to the nozzle. For this, a custom-designed plastic fixture was fabricated to secure the stainless steel sampling tube near the 3D printing nozzle for each printer. This allowed the sampling tube to move with the 3D printer nozzle while maintaining a constant distance during operation of the device in the *near* position. Although the nominal distance from the sampling port to the printing nozzle was 2.5 cm, the differences in the tool head geometries of the two printers meant the *near* distances for Printer 1 and Printer 2 were not identical. For the *far* level runs, a separate boom fixture was used to position the sampling port at a fixed position roughly 16.5 cm from the printing nozzle. Here, the stainless steel tube was not used. Instead, aerosol was sampled directly into the rubber hose connected to the NAS.

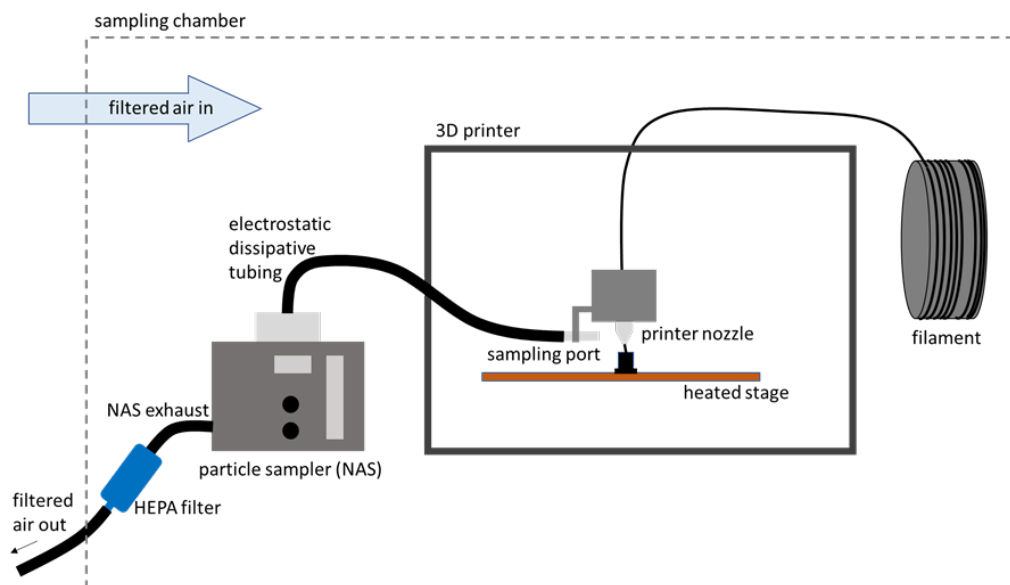


Figure 16: Basic schematic diagram of the 3D printing and sampling setup.

For the two different levels for the filament storage humidity factor (X5), we stored one set of filaments in a sealed plastic storage container along with a tray of Dreirite® desiccants and the other set in an open container within the lab environment.

Aerosol sampling was carried out using an electrostatic precipitator NAS described in Section 4.2.2. As mentioned earlier, individually packaged 1-inch (25 mm) diameter single sided polished silicon wafers were used as aerosol collection substrates for NAS sampling. Individually packaged silicon wafers were purchased to ensure they were free of any particle contamination. However, several of the silicon wafers from the batch were randomly selected and inspected in the SEM to verify their cleanliness. For each run, a clean silicon wafer was placed and centered on the electrode shown in Figure 10, schematic on the right. In the current study, the sampled air from the chamber was directed towards the center of the silicon wafer at a constant flow rate of 2.5 L/min, the maximum rate for the NAS. For all testing, the NAS electrode voltage was set to -8 kV although this was observed to fluctuated by 0.1 kV. Output flow from NAS was filtered through a HEPA filter and exhausted out of the sampling chamber.

6.3 3D test object

For the printing process during which air sampling was performed, a cylindrical object, 30 mm tall and 22 mm in diameter with a mass of about 10 grams, was printed for each run. Initially, the NIST additive manufacturing test artifact was considered for this purpose [11]. However, we found that it takes several hours to print this test object and required rapid, large lateral travel that caused sufficient air turbulence to disrupt the aerosol sampling process. In the end, a cylindrical shape was chosen because the circular cross-section would minimize the X- and -Y travel and keep the distance from sampling port to printer nozzle relatively constant. Many different sizes of cylinder were tested, and the final size chosen was a compromise between adequate particle collection and a practical run duration of roughly 30 minutes. Figure 17 shows two examples of the test objects printed using MWCNT ABS and neat ABS filaments. The test objects are top hat shaped because the larger diameter disc at the bottom of the cylinder is needed as a stable base and as an improved starting interface.

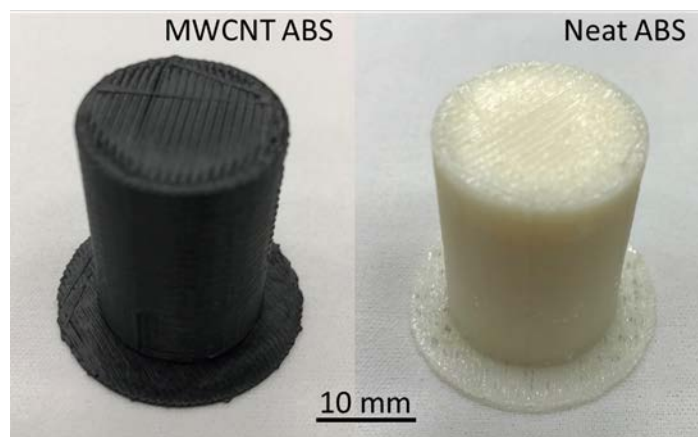


Figure 17: 3D test objects printed using MWCNT containing ABS and neat ABS.

6.4 3D printing procedure

Randomized sampling run order meant we needed to change 3D printing configurations frequently from run-to-run. For example, the first sampling was carried out while printing with Printer 2 at a low temperature using neat ABS filament kept in dry condition. The next sampling run was done while printing with Printer 1 at a low temperature using MWCNT ABS filament kept in the room condition. Under these circumstances, cleanliness was of paramount importance due to the potential for cross-contamination from run-to-run, pre-existing contamination, and other environmental factors. To that end, a rigorous cleaning regimen was developed for the 3D printing chamber and the NAS between individual runs. See Appendix 4 for the sampling chamber cleaning procedure used for this study.

After considering the time needed for each sampling run, sampling chamber reconfiguration, and cleaning, we decided to run two sampling conditions per day, one in the morning and one in the afternoon. In addition to the two sampling runs, two blank runs were performed each day, again one in the morning and one in the afternoon. Blank runs were sampling runs with a given printer and sampling port location but without the actual printing. Blanks were employed to verify the cleanliness of the system and to be used as a baseline for air quality. The entire set of 16 sampling conditions and their duplicates were carried out over a period of 4 weeks.

In summary, the procedure was carried out as follows:

1. Clean the sampling chamber.
2. Configure the printer for the next run. Load the printer with the appropriate filament and allow it to fully preheat following the protocol programmed in the manufacturer provided software.
3. While the printer was heating, load a new silicon wafer into the NAS.
4. Once the printer reached the set temperature, start air sampling via the NAS few minutes before starting the printing process.
5. Stop the NAS sampling few minutes after printing is completed.

After each run (printing or blank), the silicon wafer used to collect release particles was returned to the original wafer carrier and labelled with the date and time (AM or PM) of the run. Wafer carriers are specifically designed for storage, transport and handling of semiconductor wafers to minimize surface contamination. Labelled wafer carriers were stored in the laboratory until SEM analysis of the wafers could be performed.

7 SCANNING ELECTRON MICROSCOPY (SEM)

7.1 SEM Imaging

SEM analysis of the NAS sampled release particles was performed using a FEI Helios NanoLab 660 Focused Ion Beam Scanning Electron Microscope (FIB SEM). Both high resolution imaging and tile imaging were performed. It should be noted that no carbon coating was added to the wafer samples prior to SEM imaging. FEI large area imaging software MAPS¹ was used to perform tile imaging. Most imaging was performed at 3 keV, 0.1 nA electron beam conditions. For tile imaging and low resolution survey imaging, secondary electron (SE) images were collected using the Everhart-Thornley detector in a non-immersion mode. For high resolution images of select locations and individual particles, SE imaging with a through-the-lens detector in immersion mode was used. For detailed procedures and imaging conditions, see Appendix 6.

Total of 64 silicon wafers were used as substrates in the NAS to collect released particles from the 32 printing runs and 32 blank runs. All 32 of the silicon wafers from the printing runs and 8 from the blank runs were analyzed by SEM. *To avoid confusion, we will use the term 'sample wafer' to mean a silicon wafer used in a printing run and 'blank wafer' to denote a silicon wafer used in a blank run.*

7.2 Large area tile imaging

To survey a large area of the sample (in this case, wafer) surface, MAPS imaging software was employed. MAPS enables automated tile imaging of a given surface using a set of predefined conditions and then stitches them back together into a large area map of the surface. The goal of MAPS tile imaging was to survey a sufficiently large area of a sample wafer to assess the number concentration and size distribution of respirable particles (particles with diameter less than 10 μm) collected on the surface of the silicon wafer for each sampling condition [12].

For each wafer, a 50 image x 50 image tile set (total of 2500 tile images) with 10 % tile overlap was performed. The tile set covered approximately 18 mm x 12 mm region of the 25 mm diameter wafer as depicted in Figure 18 (upper left). The horizontal field width (HFW) and the pixel dimensions of each tile image were 400 μm and 3072 x 2048, respectively, resulting in pixel size of ≈ 130 nm. In Figure 18, lower left panel shows a single SEM image tile, and the right panel shows a stitched image of an entire tile set. The entire tile set took roughly 10 hours to image for each wafer. As previously stated, the detection of respirable particles was the focus of the MAPS imaging and the detection of individual MWCNTs was not feasible using the imaging conditions applied for MAPS imaging.

¹ MAPS is the name of a software package for large area imaging and is not an acronym.

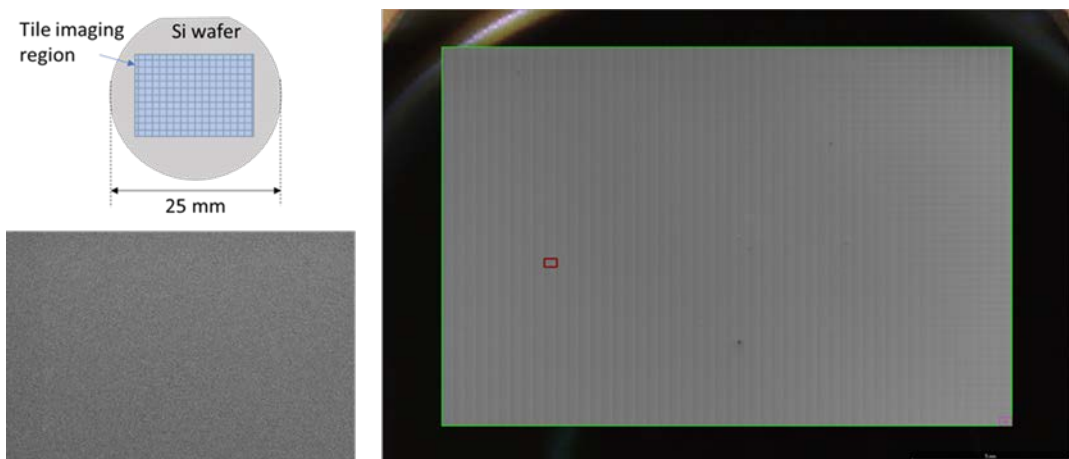


Figure 18: (upper left) Diagram of a silicon wafer substrate and the region to be imaged; (lower left) 400 μm HFW SEM image; (right) stitched image.

To minimize any systematic bias in SEM imaging, the order with which sample wafers were imaged was also randomized. See Appendix 6 for the randomized wafer imaging order. Blank wafers were imaged using the same tile imaging settings, but the imaging order was not randomized. As noted earlier, although 32 blank wafers were created during the sampling phase, only 8 blank wafers were analyzed due to time and resource constraints.

7.3 High resolution imaging

As mentioned in the previous section, pixel size of MAPS tile images was ≈ 130 nm. Individual MWCNTs would be less than one pixel wide and not detectable in these images. To detect individual MWCNTs or small clusters of MWCNTs and polymer fragments, higher resolution imaging was necessary. For example, to detect a single MWCNT of 30 nm in diameter, we would want our image pixel size to be much less than 30 nm, say 5 nm. 5 nm pixel size means roughly 15 μm horizontal field width for each image assuming 3072 x 2047 image dimensions. To inspect the same regions of the wafer as the MAPS imaging covered at this resolution, we would need more than 1.7 million images. Clearly, high resolution imaging of a large area of the wafers is not feasible. Instead, we divided the wafer into 16 non-overlapping regions by partitioning the wafer into octants which were further partitioning into inner and outer segments. Then, a random location from each of the 16 regions was selected for high resolution imaging. An additional two locations near the center of the wafer were also chosen for imaging because the wafer's center is where the flow of aerosolized particles was directed. Therefore, for each wafer, total of 18 high resolution images were collected. Although this approach provided no statistical power, it forced us to examine the entire wafer rather than scan around one or two tiny regions of the wafer at very high resolution imaging conditions.

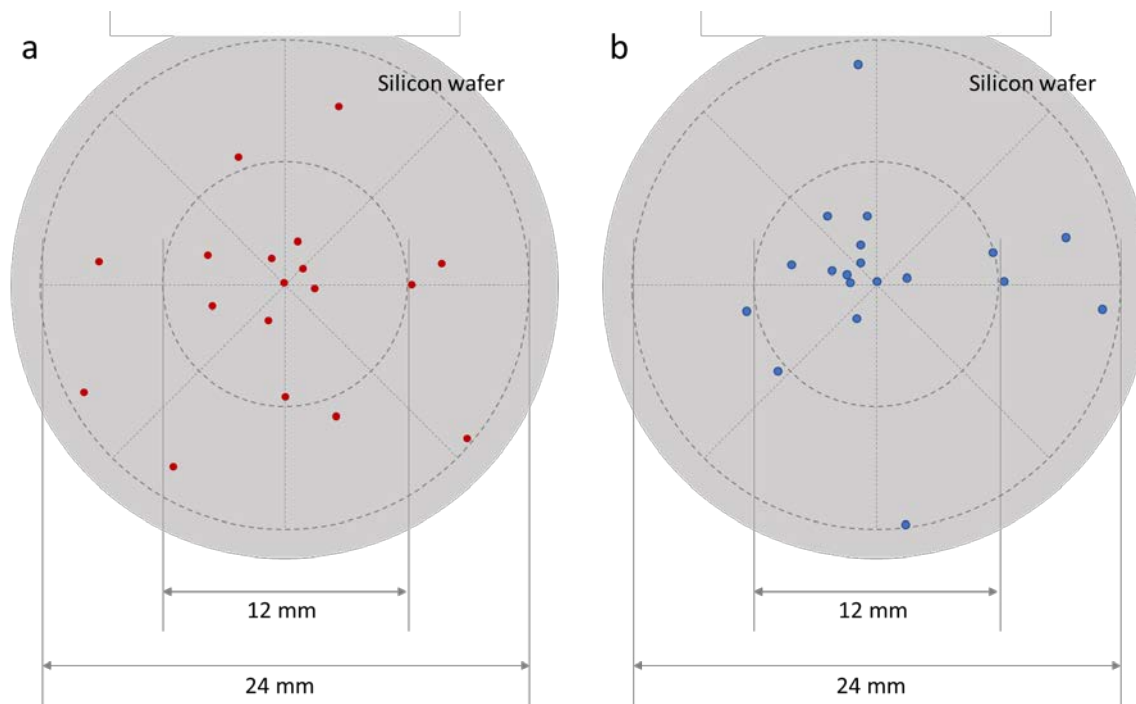


Figure 19: Representative diagram of the sampling protocol proposed (left) and employed (right) to evaluate a sampling of the silicon wafers via high resolution imaging. Red dots represent an imaging location and the lines represent borders for the regions.

Figure 19a depicts the randomized sampling scheme devised for high resolution imaging of the silicon wafers. In determining the imaging locations, only the inner 24 mm diameter region of the wafer was considered since the outer edge of the wafer is likely to be disturbed during handling. Due to an error in location calculation, actual high resolution imaging was carried out using the scheme shown in Figure 19b. Here, imaging locations are concentrated more in the inner (center) region of the wafer. Fortunately, our analysis of test wafers showed that the majority of particles collected using NAS are in the regions closer to the center.

In addition to the 18 high resolution images from pre-defined locations, a manual survey of each wafer was performed to find and image individual particles of interest.

8 IMAGE ANALYSIS

8.1 Automated image processing

Total of 100,000 SEM images collected using MAPS tile imaging were processed through image analysis for subsequent determination of release particle size distribution and number density. Of these, 80,000 images were from the sample wafers and 20,000 were from the blank wafers.

Image stacks from the sample and blank wafers were processed using FIJI [13] to determine the particle size distributions. Each image stack consisted of 2500 images spanning 18 mm by 12 mm rectangular region of a wafer. The basic image processing steps performed for each image stack were:

1. Resize the image to account for 10 % tile overlap.
2. Apply smoothing operation.
3. Apply thresholding to generate binary masks for particles.
4. Analyze particles for pixel area and circularity.
5. Write particle analysis data to a text file.

Since single pixel noise in the images were removed during the smoothing and filtering operations, no particle size exclusion was applied during the Analyze step (step 4). The output of the FIJI script was a text file listing particle sizes (in pixel) from all 2500 images in the stack. Custom FIJI scripts used in this study can be found in Appendix 7.

The automated particle segmentation based on thresholding worked for most of the tile images. However, subtle intensity gradient caused severe segmentation artifact in 64 out of 80,000 images and these images were excluded from the analysis. Figure 20 shows an example of such an artifact. Although the original SEM image (left) appears to have a uniform background intensity, the mean gray value at the upper left corner of the image (gray value of 59) is slightly lower than the mean gray value at the lower right corner of the image (gray value of 73). Because there is no particle in this image, smoothing and thresholding steps magnify the effects of the subtle intensity gradient, resulting in the binary image shown on the right.

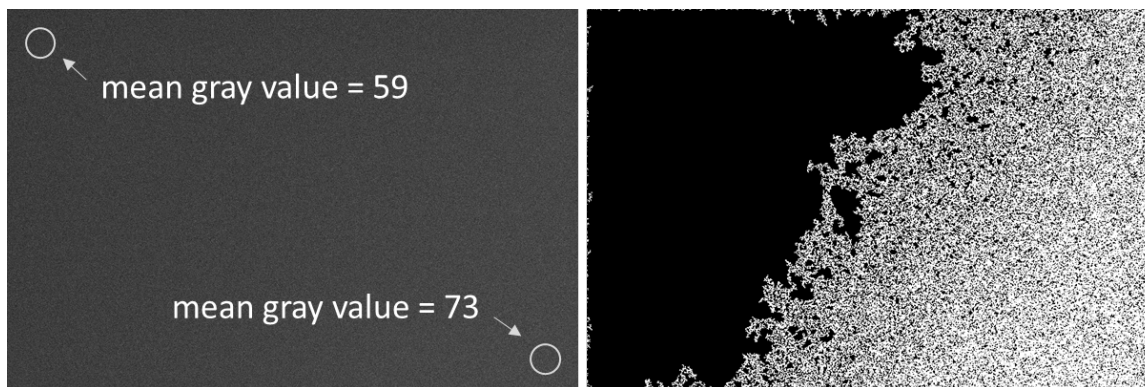


Figure 20: Original SEM image from RunID 03, tile row 2 and column 18 (left) and the resulting binary image (right) showing an example of segmentation artifact. Mean gray values indicated in the left panel are measured from the circular areas at the upper left and the lower right corners as indicated.

Figure 21 shows a typical SEM image (a) and the corresponding binary image (b) generated using the custom FIJI image processing routine. To aid the reader, magnified views of the red rectangular regions in the SEM and binary images are also included. Here it can be seen that

the custom FIJI routine can correctly segment the particles seen in the SEM image (small white features in the magnified panels in Figure 21a) and generate a corresponding binary image with the same particles (small black features in the magnified panels in Figure 21b).

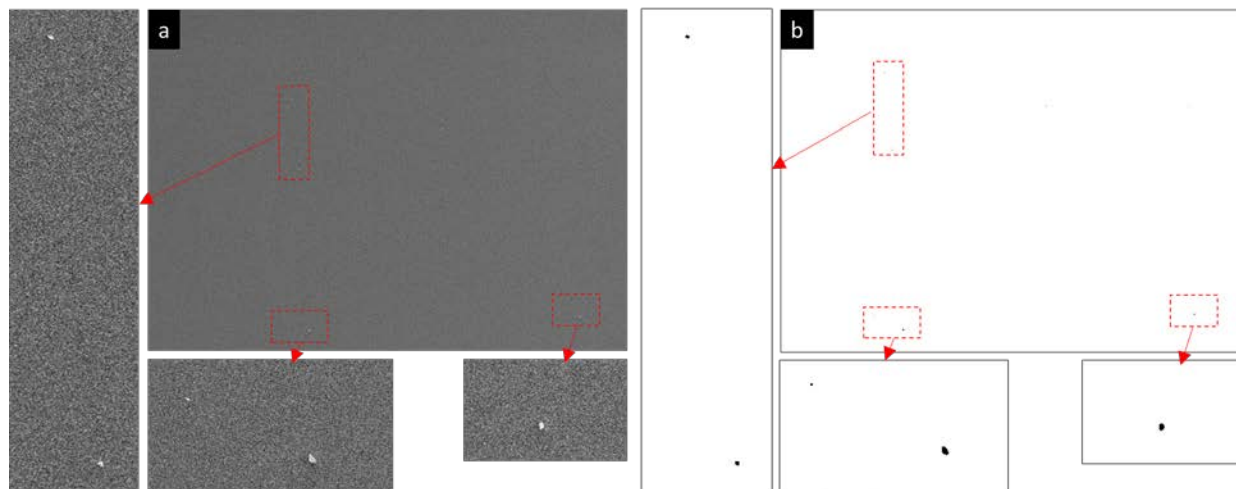


Figure 21: Example SEM (a) and binary (b) image pairs.

8.2 High resolution image analysis

There were only about 800 high resolution images collected from the sample and blank wafers and we examined them manually. Not all images contained visible particles and no individual MWCNTs were found in these images.

9 RESULTS AND DISCUSSION

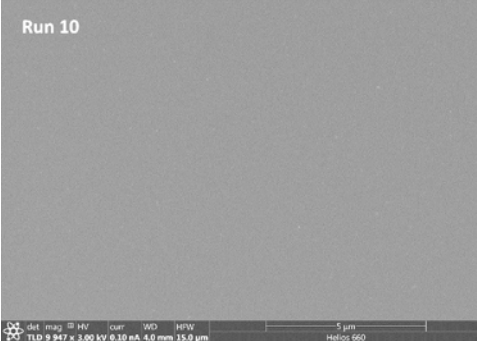
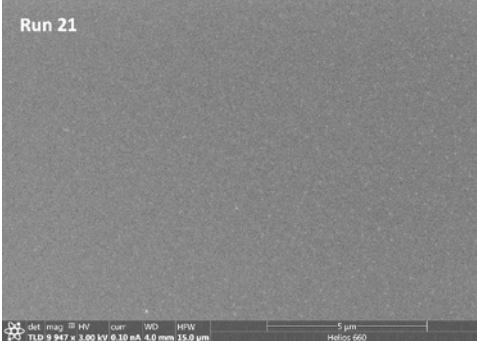
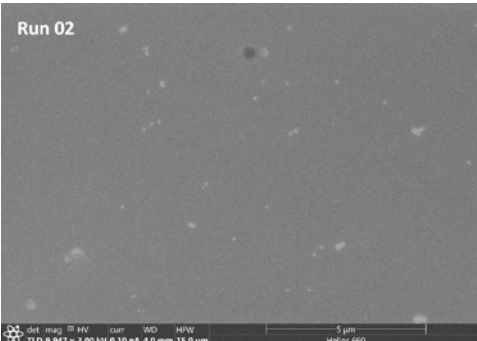
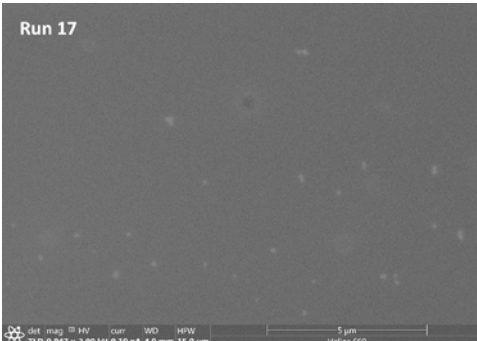
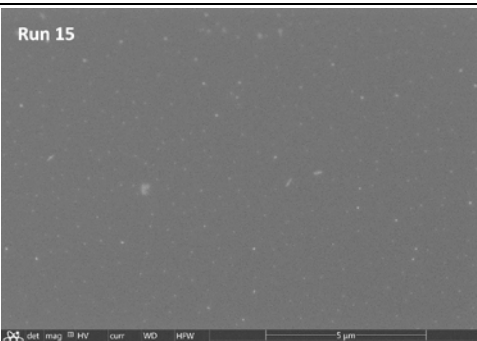
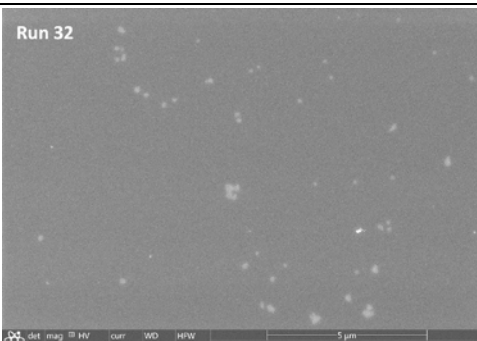

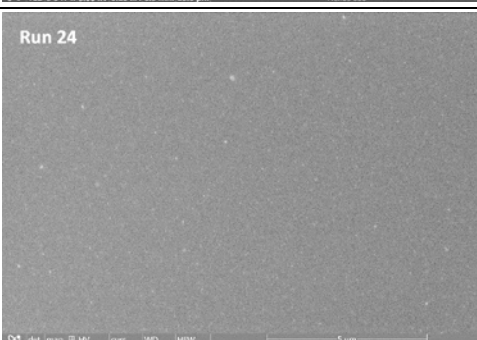
9.1 High resolution imaging results

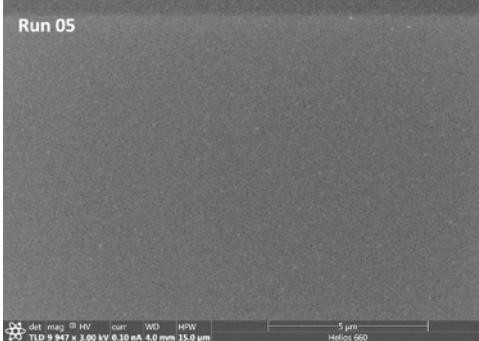
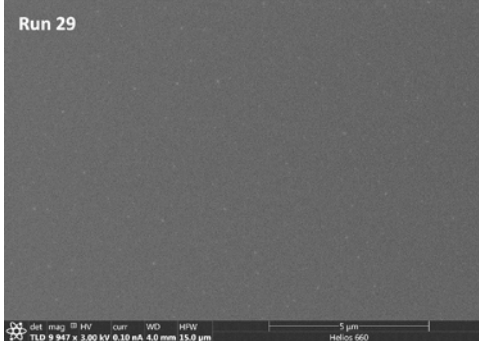
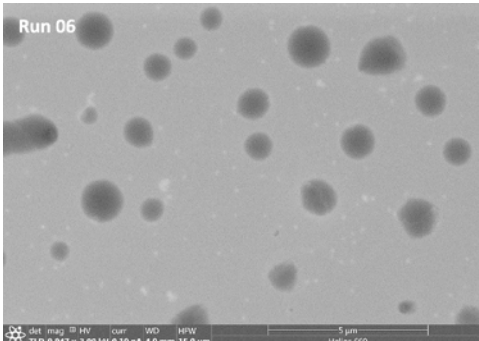
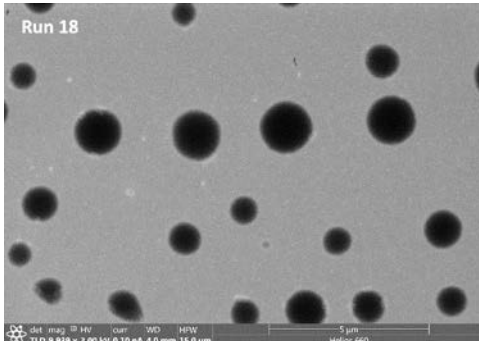
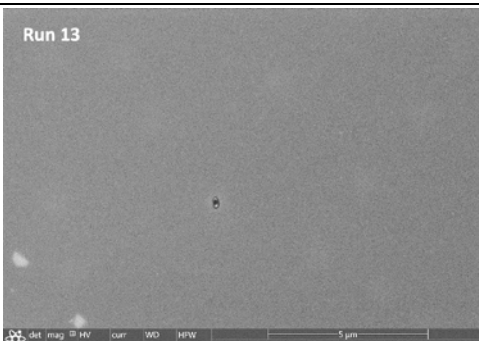
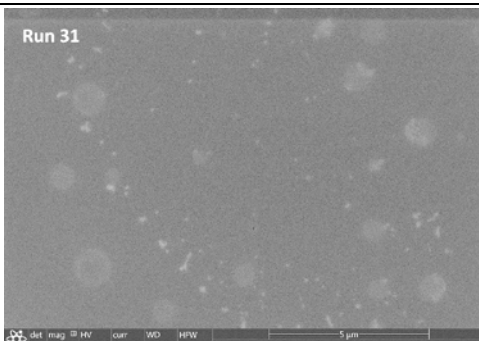
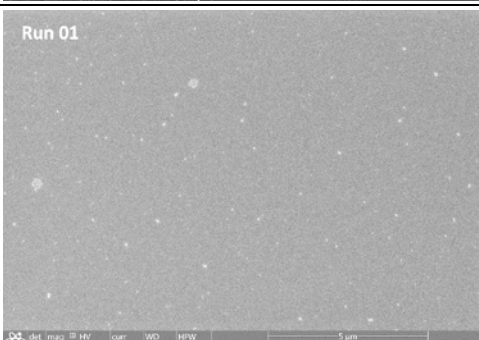
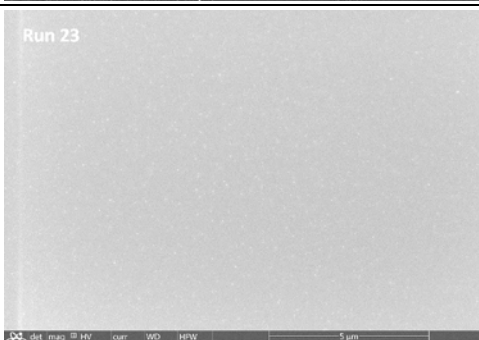
Although no individual MWCNTs were found in the high resolution image sets and many of the images contain no visible particles, they still provided interesting details about material release during 3D printing process for different printing and sampling configurations. Table 5 displays pairs of high resolution SEM images from each of the 16 different 3D printing configurations. Each row contains replicate 1 and replicate 2 high resolution images collected from the pre-defined imaging location 9. Since the aerosol deposition exhibits radial symmetry, by selecting images from the same location, we are comparing images from a comparable radial distance from the center of the wafer. And the difference in particle number density, particle size, or the background features could indicate the differences arising from variations in release behavior.

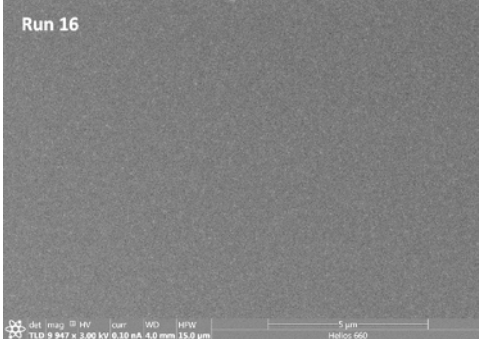
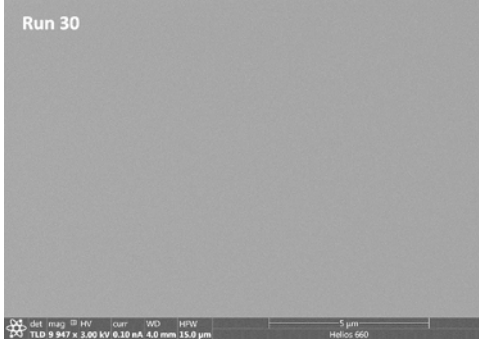
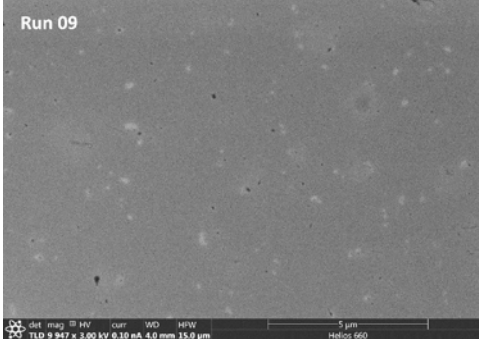
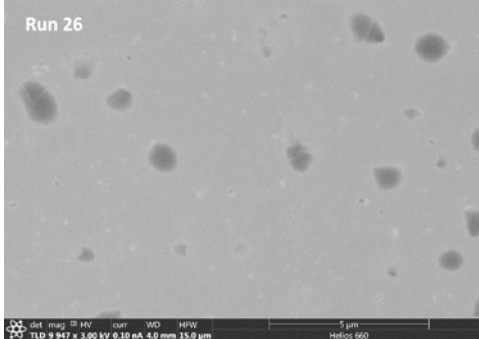
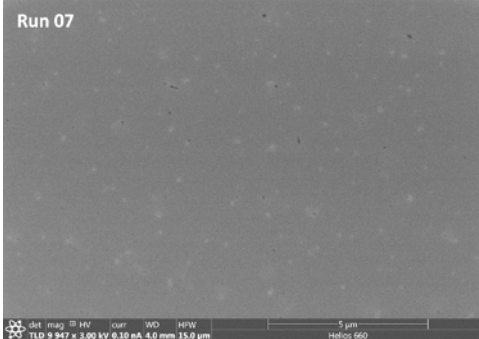
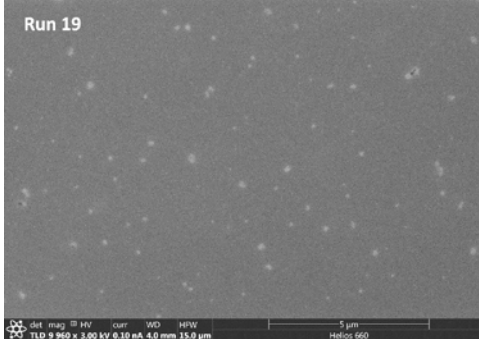
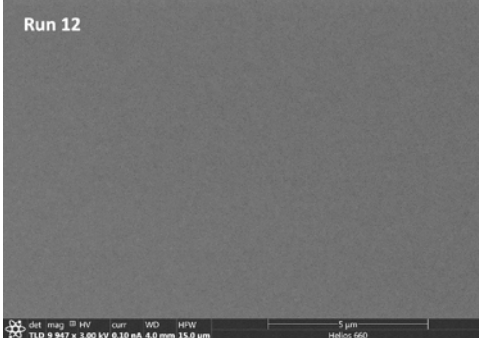
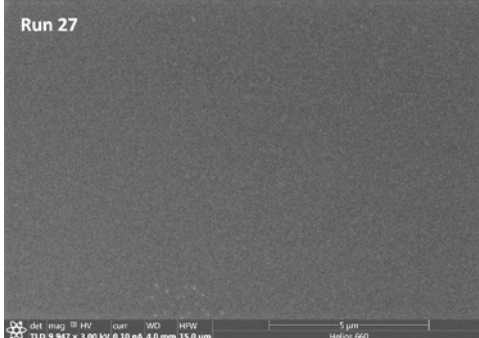
In this naive approach, it is difficult to analyze how different experimental factors interact with each other. However, some general observations and trends could be gleaned from the sets of images. First, Table 5 shows overall consistency between replicate 1 and replicate 2 results. This is most noticeable for C09 where both replicates show large dark circular features. We

suspect these are dried residues of large volatile droplets that hit the wafer surface. Although we see signs of smaller droplets in other configurations, C09 replicates are the only ones with such large droplets and in both replicates. A second observation was that the ultrafine particle number density decreased with sampling distance, which was true in all cases except C11. Lastly, while differences between neat ABS and MWCNT ABS filaments are harder to tease out, it appears that neat ABS filament wafers showed a higher particle number density. It should be noted that some of the bright and dark smudges visible on these images (e.g. C13 and C14 images) are not particles but dried volatiles or imaging artifacts caused by surface residues.

| Configuration | Replicate 1 | Replicate 2 |
|--|-------------|-------------|
| C01 Printer 1 Neat ABS Near 240 °C RT | | |
| C02 Printer 1 Neat ABS Near 250 °C Dry | | |
| C03 Printer 1 Neat ABS Far 240 °C Dry | | |

| Configuration | Replicate 1 | Replicate 2 |
|---|---|--|
| <p>C04 Printer 1 Neat ABS Far 250 °C RT</p> | <p>Run 10</p>  | <p>Run 21</p>  |
| <p>C05 Printer 1 MWCNT ABS Near 240 °C RT</p> | <p>Run 02</p>  | <p>Run 17</p>  |
| <p>C06 Printer 1 MWCNT ABS Near 250 °C Dry</p> | <p>Run 15</p>  | <p>Run 32</p>  |
| <p>C07 Printer 1 MWCNT ABS Far 240 °C Dry</p> | <p>Run 14</p>  | <p>Run 24</p>  |

| Configuration | Replicate 1 | Replicate 2 |
|--|---|--|
| <p>C08 Printer 1 MWCNT ABS Far 250 °C RT</p> | <p>Run 05</p>  | <p>Run 29</p>  |
| <p>C09 Printer 2 Neat ABS Near 240 °C RT</p> | <p>Run 06</p>  | <p>Run 18</p>  |
| <p>C10 Printer 2 Neat ABS Near 260 °C Dry</p> | <p>Run 13</p>  | <p>Run 31</p>  |
| <p>C11 Printer 2 Neat ABS Far 240 °C Dry</p> | <p>Run 01</p>  | <p>Run 23</p>  |

| Configuration | Replicate 1 | Replicate 2 |
|---|---|--|
| <p>C12 Printer 2 Neat ABS Far 260 °C RT</p> | <p>Run 16</p>  <p>5 µm Hitachi 660</p> | <p>Run 30</p>  <p>5 µm Hitachi 660</p> |
| <p>C13 Printer 2 MWCNT ABS Near 240 °C RT</p> | <p>Run 09</p>  <p>5 µm Hitachi 660</p> | <p>Run 26</p>  <p>5 µm Hitachi 660</p> |
| <p>C14 Printer 2 MWCNT ABS Near 260 °C Dry</p> | <p>Run 07</p>  <p>5 µm Hitachi 660</p> | <p>Run 19</p>  <p>5 µm Hitachi 660</p> |
| <p>C15 Printer 2 MWCNT ABS Far 240 °C Dry</p> | <p>Run 12</p>  <p>5 µm Hitachi 660</p> | <p>Run 27</p>  <p>5 µm Hitachi 660</p> |

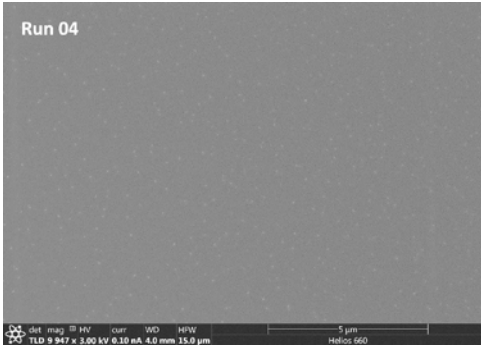
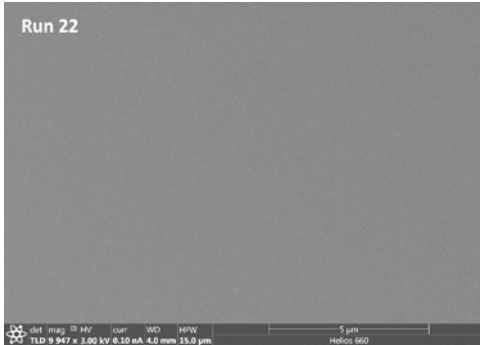
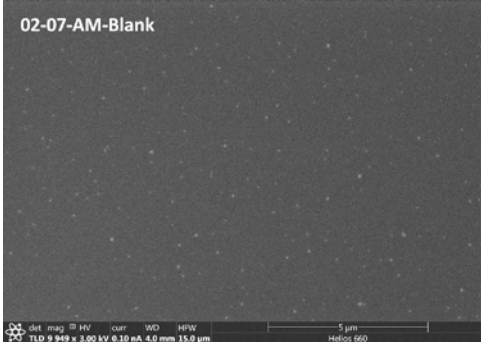
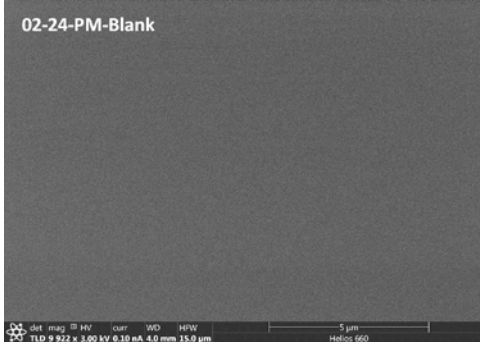
| Configuration | Replicate 1 | Replicate 2 |
|--|---|--|
| C16 Printer 2 MWCNT ABS Far 260 °C RT | Run 04  | Run 22  |
| Blank Rep1: Printer 1 Rep2: Printer 2 | 02-07-AM-Blank  | 02-24-PM-Blank  |

Table 5: High resolution location 9 images from replicate 1 and replicate 2 sample wafers from all 16 configurations and a couple of the blank wafers.

9.2 Manual imaging results

In addition to the high resolution SEM images collected from the 18 pre-defined imaging locations, manual survey of the sample wafers was carried out to find additional particles of interest. The manual high resolution imaging was mainly focused on searching for individual MWCNTs and particles containing MWCNTs. We found two classes of particles: particles with smooth surfaces and particles with rough surfaces. Figure 22 shows several examples of the smooth surfaced particles. Particle dimensions ranged from few micrometers to tens of micrometers although we found some particles as small as 150 nm in diameter. Some were spherical in shape while others have elongated or irregular shapes. Smooth surface and rounded shape indicate that these particles are formed as molten ABS polymer droplets solidified.

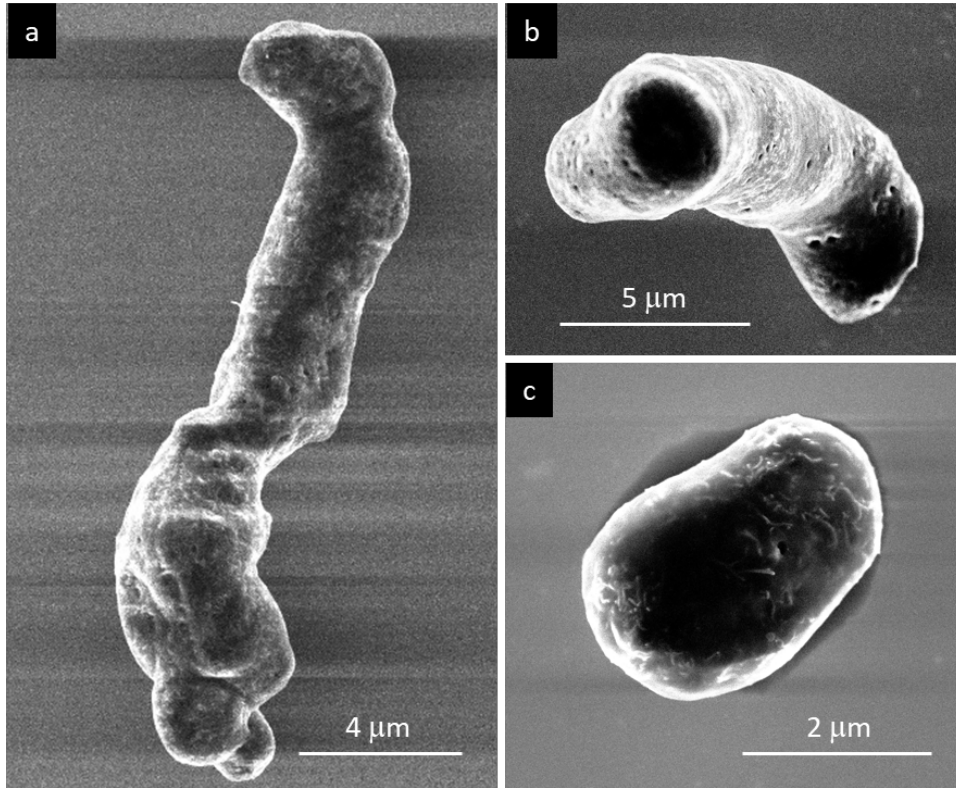


Figure 22: Examples of released particles found during manual imaging of the sample wafers during 3D printing with MWCNT ABS filaments from a) Run 04, b) Run 32, and c) Run 02.

The other class of particles had rough surface morphology and very irregular shapes. Figure 23 shows several examples of these. Typically, these particles were much larger than the smooth particles and often several tens of micrometers long. Although both the MWCNT and the neat ABS filament particles exhibited charging artifacts during imaging, the presence of MWCNTs helped to mitigate the charging problem with the MWCNT ABS particle samples. Since the charging problem was very severe with neat ABS, as shown in Figure 23b, we were not able to document many of these particles.

Figure 24 shows high resolutions images of a smooth particle and a rough particle. The smooth surfaced particles we found all showed numerous embedded MWCNTs and occasional protruding MWCNTs. Rough particle surfaces were often covered in protruding MWCNTs. Upon closer inspection, the surfaces of the rough particles also contain numerous embedded MWCNTs but these were not as readily detected due to protruding MWCNTs.

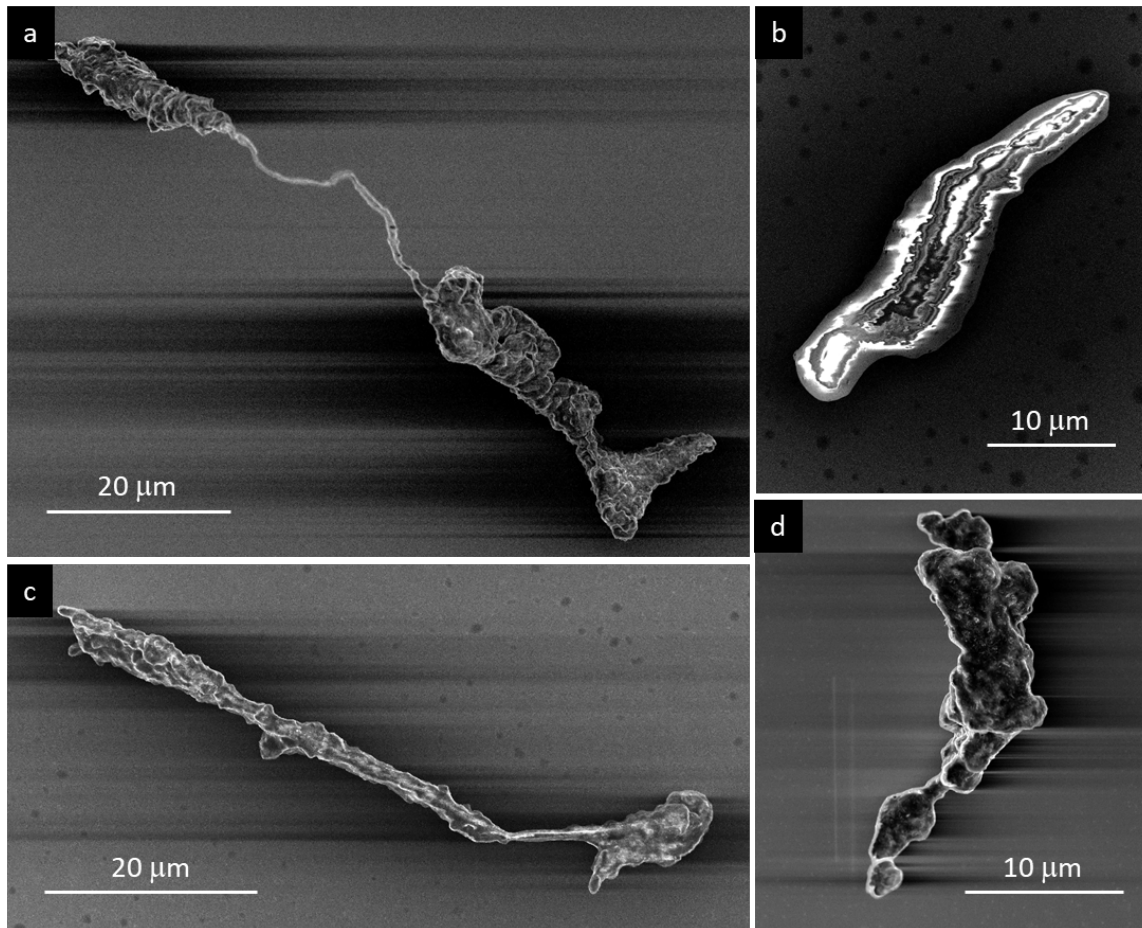


Figure 23: Examples of particles found during manual imaging of the sample wafers during 3D printing with neat ABS or MWCNT ABS filaments from a) Run 07, b) Run 06, c) Run 26 and d) Run 07.

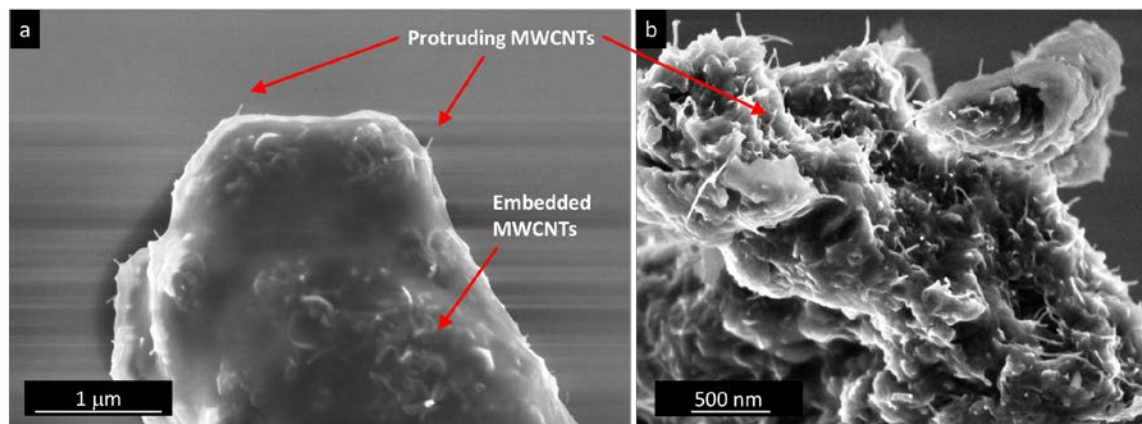


Figure 24: High resolution images of a) a rounded particle and b) a rough particle showing embedded MWCNTs and protruding MWCNTs.

9.3 Automated image analysis results

As described in Section 8.1, MAPS tile images from all 32 sample wafers and 8 blank wafers were processed, segmented, and run through the built-in Analyze Particle routine. Number of particles per image, pixel area per particle, and particle circularity were measured for each image. To calculate the particle size, number of pixels for each particle was converted to area in nm² and equivalent circular area diameter was calculated from the particle area value. Although there were few very large particles, only the respirable fraction of particles (diameters < 10 μm) were included in the analysis.

First, we examined the total particle counts determined from the tile images from each run in the order the particles were sampled. Figure 25 shows the plot of the total particle counts plotted against the run order. Unusually high particle counts for the Run 13 results skewed the average particle count and particle counts from more runs fall below the average (dashed orange line in Figure 25) than above. The first four runs show a slight downward trend, and the two last run results are noticeably higher than average, but there does not seem to be any obvious trend for the rest of the runs.

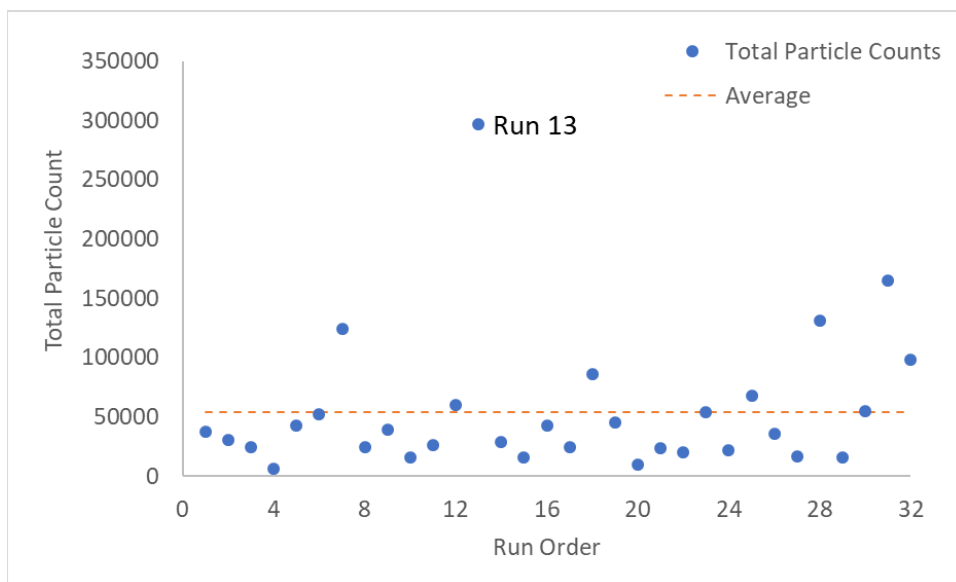


Figure 25: Run order plot showing the total particle counts from each configuration in the order they were sampled.

Figure 26 shows the summary of the total particle counts from the sample wafers and the blank wafers. Blank wafer data are plotted next to the sample run performed on the same day as the blank run. In several cases (C01 Rep1, C07 Rep2, and C16 Rep1), blank run particle counts are on the same order of magnitude as the sample run results, suggesting in those instances that the respirable particle number was at baseline. Agreement in particle counts between replicate runs were varied. In configurations C01, C03, C06, C14, and C15, agreement between the two replicates is poor and the counts from the replicate runs differed by a factor of two or more.

Particle counts from C10 were significantly higher than the rest. However, since the sampling run order was randomized, there does not seem to be any systematic pattern in the total particle count results or obvious cause for the poor consistency between replicate runs.

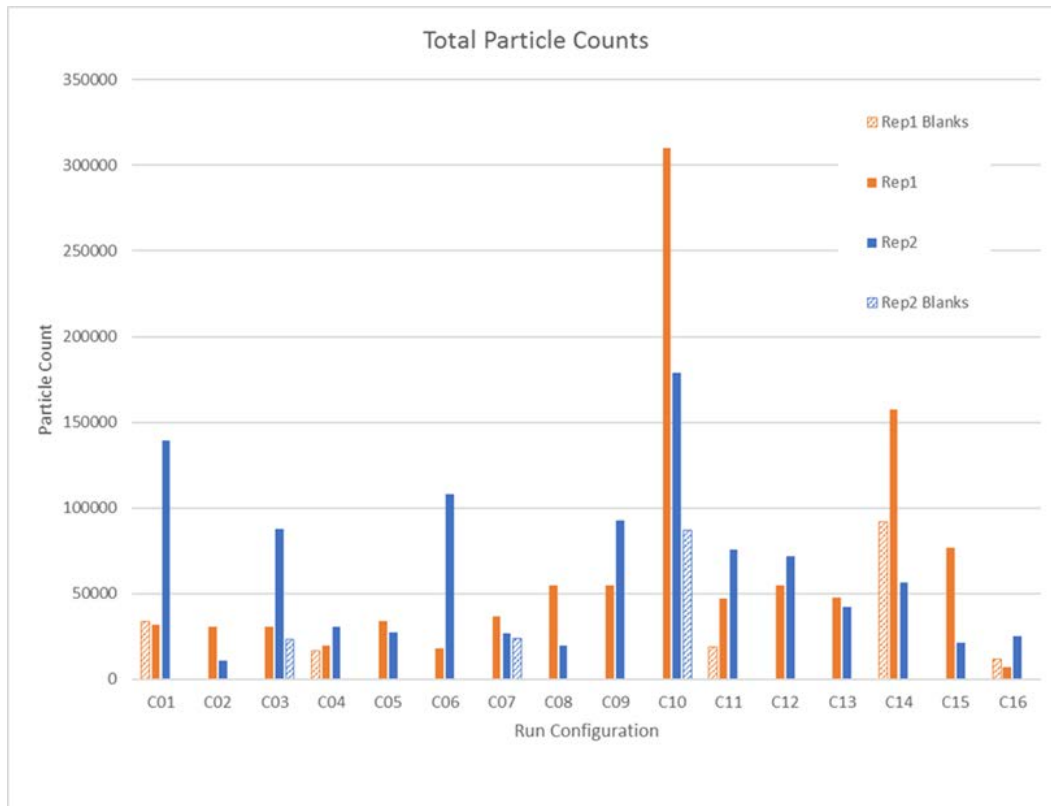


Figure 26: Total particle counts from the tile images obtained from sample and blank wafers. C01 through C16 represent the different experimental configurations specified in Table 4.

The next 5 figures (Figures 27 – 31) show the normalized particle size distribution plots for the 32 sample wafers and 8 blank wafers. For readability, the number of particles in each size bin (100 nm binning interval) was normalized against the total particle count. For easier comparison, the plots were grouped by the 3D printer type (Printer 1 and 2) and the replicate number (Rep1 and Rep2). Blank run particle distribution plots are shown separately. Although particles with diameter up to 10 μm were included in the analysis, the number of particles larger than 2 μm in diameter were negligibly small in all cases. Here, we only plotted the particle diameter up to 2 μm .

Replicate 1 results for the Printer 1 cases (Figure 27) showed very similar particle size distributions among different experimental configurations (C01 to C08). All showed a peak around 300 nm and most of the particles have diameter less than 600 nm. The one exception was C06 which had a faint shoulder on the 300 nm feature indicative of a peak near 500 nm. For the replicate 2 results for the Printer 1 cases (Figure 28), C03, C04, C05, C07, and C08 showed particle size distribution plots similar to those seen in replicate 1

samples. However, C01 and C06 results showed a main peak at 300 nm and a smaller shoulder suggesting an overlapping peak around 500 nm. C02 result showed overlapping peaks at 300 nm and around 700 nm.

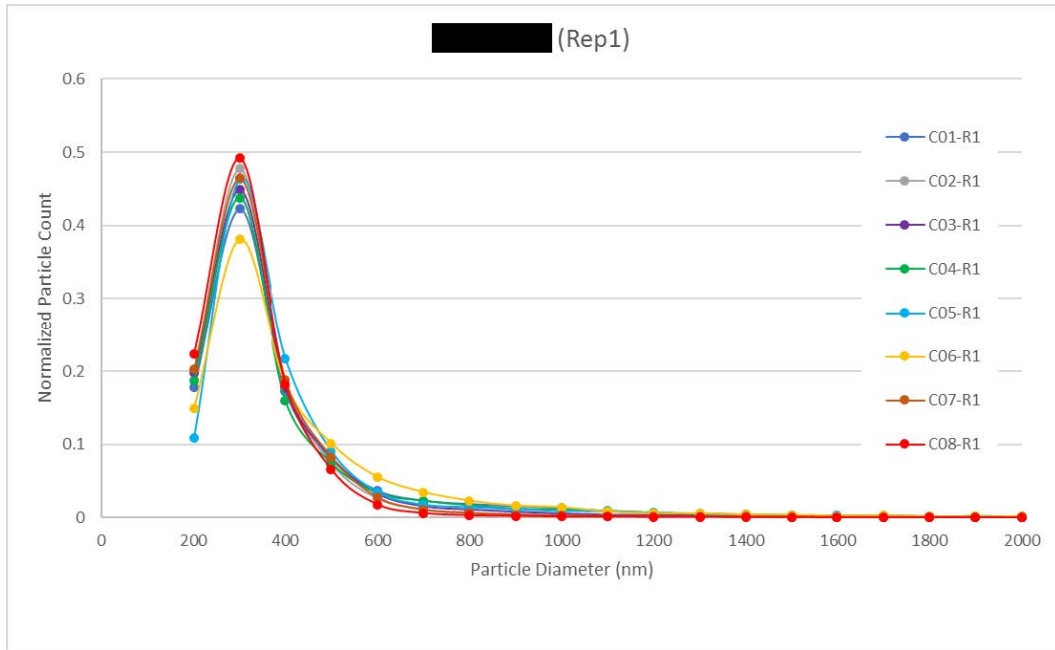


Figure 27: Normalized particle size distribution for Printer 1 replicate 1 sampling runs.

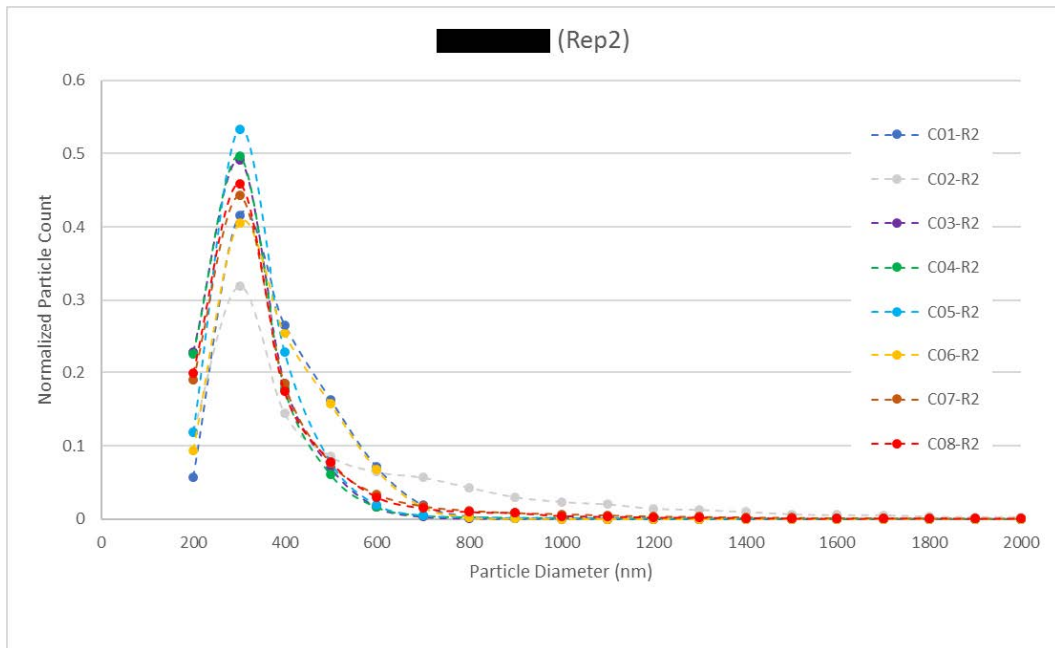


Figure 28: Normalized particle size distribution for the Printer 1 replicate 2 sampling runs.

C11 through C16 results from replicate 1 runs of the Printer 2 cases (Figure 29) showed very similar particle size distributions as those from the replicate 1 runs of the Printer 1 cases. They showed a major peak around 300 nm and most of the particles have diameter less than 600nm.

However, both C09 and C10 results showed overlapping peaks around 500 nm similar to those from C01 and C06 of replicate 2 runs of Printer 1 cases. Further, the overlapping peak around 500 nm was more pronounced in the TAZ5 cases and C10 peaks were higher than C09 peaks. Replicate 2 results for the Printer 2 cases (Figure 30) showed particle size distribution plots very similar to those from the replicate 1 samples.

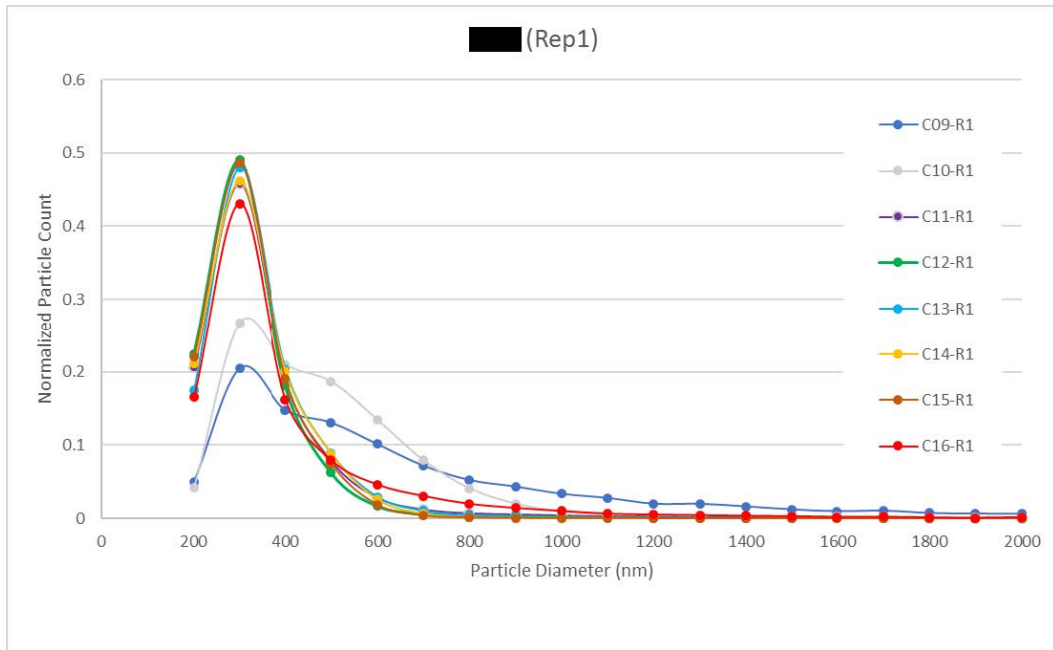


Figure 29: Normalized particle size distribution for the Printer 2 replicate 1 sampling runs.

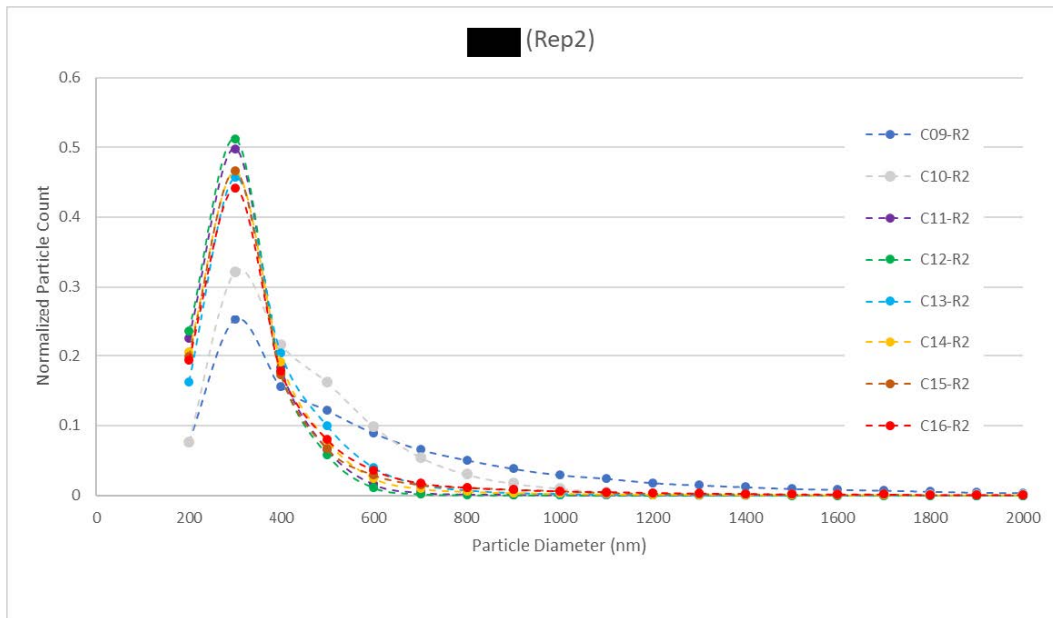


Figure 30: Normalized particle size distribution for the Printer 2 replicate 2 sampling runs.

Particle size distribution plots for the blank samples (Figure 31) were similar to those from the replicate 1 runs of the Printer 1 cases. A small overlapping peak is indicated in the B01-31A plot. This blank run was performed immediately prior to the C11-R1 run shown in Figure 29 which did not show the same overlapping shoulder.

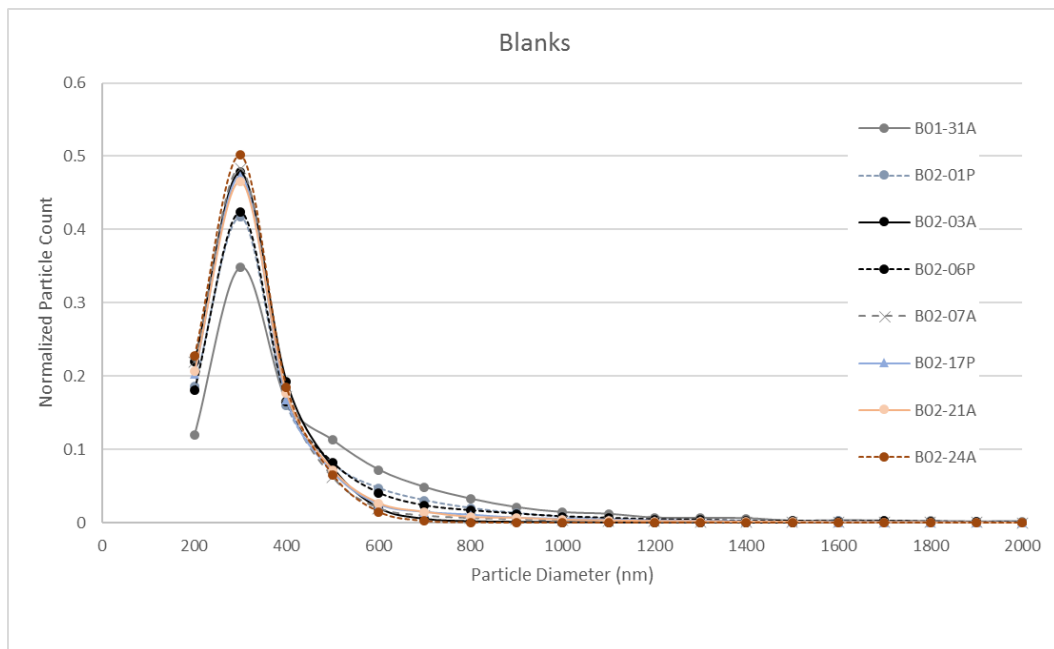


Figure 31: Normalized particle size distribution for the blank runs. B01-31A denotes blank run from the January 31st, morning (AM) session while B02-06P represents the blank run from the February 6th, afternoon (PM) session.

Overall, particle size distribution plots were similar to each other and did not indicate obvious effects from any of the experimental factors considered. The only pattern detected was that *C09 and C10 results, and to a lesser degree C06 results, consistently showed different particle size distributions than the rest in that there was a major peak around 300 nm and another one around 500 nm* while the rest of the results showed only one peak around 300 nm. Although the secondary peaks were seen in several other experimental configurations, namely C01 and C02, these results were not replicated.

This conclusion is also supported by the correlation coefficient (r) matrix (Table 6) derived from the mean normalized particle counts matrix where the Blank column is the averages of the normalized particle counts from all 8 blank runs and the sample run columns (C01 to C16) are the averages of the replicate 1 and replicate 2 normalized particle counts. The correlation coefficient is a measure of the association between two variables [14]. If two variables are highly correlated or vary in a similar manner, the correlation coefficient is close to 1 or -1. If two variables are uncorrelated, the correlation coefficient is close to 0.

In our study, if two experimental configurations have similar effect on the resulting particle size distributions, the correlation coefficient between them is close to 1 (green). If two configurations have different particle size distributions, the correlation coefficient between these two configurations is significantly less than 1 (orange/red). Although the absolute range of the correlation coefficients are relatively small in our case, the *r* matrix clearly highlights the C09 and C10 results as being ‘different’ from others and C01, C05, and C06 to a lesser degree.

| | Blank | C01 | C02 | C03 | C04 | C05 | C06 | C07 | C08 | C09 | C10 | C11 | C12 | C13 | C14 | C15 | C16 |
|-------|----------|----------|----------|----------|----------|----------|----------|----------|----------|----------|----------|----------|----------|----------|----------|----------|-----|
| Blank | 1 | | | | | | | | | | | | | | | | |
| C01 | 0.974791 | 1 | | | | | | | | | | | | | | | |
| C02 | 0.997615 | 0.983759 | 1 | | | | | | | | | | | | | | |
| C03 | 0.999456 | 0.970536 | 0.995013 | 1 | | | | | | | | | | | | | |
| C04 | 0.999217 | 0.967036 | 0.994867 | 0.999466 | 1 | | | | | | | | | | | | |
| C05 | 0.979493 | 0.990814 | 0.985282 | 0.976559 | 0.976333 | 1 | | | | | | | | | | | |
| C06 | 0.9705 | 0.998907 | 0.980328 | 0.965884 | 0.961304 | 0.983561 | 1 | | | | | | | | | | |
| C07 | 0.999654 | 0.977977 | 0.997393 | 0.999383 | 0.998511 | 0.981855 | 0.973897 | 1 | | | | | | | | | |
| C08 | 0.999436 | 0.969134 | 0.994964 | 0.999898 | 0.999811 | 0.976773 | 0.963945 | 0.999129 | 1 | | | | | | | | |
| C09 | 0.869518 | 0.93767 | 0.898591 | 0.855693 | 0.850783 | 0.896791 | 0.947197 | 0.87156 | 0.852994 | 1 | | | | | | | |
| C10 | 0.852669 | 0.93589 | 0.880322 | 0.84004 | 0.83209 | 0.889071 | 0.946941 | 0.857065 | 0.836278 | 0.990381 | 1 | | | | | | |
| C11 | 0.999188 | 0.969311 | 0.994419 | 0.999934 | 0.999504 | 0.976505 | 0.964307 | 0.999187 | 0.999904 | 0.851685 | 0.83596 | 1 | | | | | |
| C12 | 0.997506 | 0.959946 | 0.990857 | 0.998908 | 0.999318 | 0.971354 | 0.953684 | 0.99697 | 0.999266 | 0.832884 | 0.814924 | 0.99924 | 1 | | | | |
| C13 | 0.99587 | 0.990108 | 0.997082 | 0.994394 | 0.992945 | 0.991906 | 0.98612 | 0.997209 | 0.993931 | 0.893503 | 0.884006 | 0.993967 | 0.989677 | 1 | | | |
| C14 | 0.998884 | 0.9764 | 0.995443 | 0.999336 | 0.997796 | 0.979287 | 0.972719 | 0.999639 | 0.998819 | 0.865819 | 0.853285 | 0.999192 | 0.996948 | 0.996316 | 1 | | |
| C15 | 0.99942 | 0.970183 | 0.995145 | 0.999878 | 0.999725 | 0.977949 | 0.964939 | 0.999286 | 0.999963 | 0.853919 | 0.837591 | 0.999931 | 0.999176 | 0.994432 | 0.998989 | 1 | |
| C16 | 0.9995 | 0.979514 | 0.999133 | 0.997998 | 0.997929 | 0.983228 | 0.975386 | 0.999131 | 0.998029 | 0.882232 | 0.865266 | 0.997573 | 0.995133 | 0.997144 | 0.997727 | 0.998089 | 1 |

Table 6: Correlation coefficient matrix for the mean normalized particle size distributions from the blank and sample runs. Cell color coding ranges from strong correlation in green to medium correlation in yellow to low correlation in red.

Although several of the experimental configurations resulted in slightly different release particle size distributions than the rest, we were unable to determine which experimental factor or combination of factors were responsible for these differences. For the subsequent effects analysis, we selected the total particle count as our main response variable in determining the experimental factors that have the most impact on the release during 3D printing. Note the experimental factors and their levels are defined in Section 5.1 Table 3. Figure 32 is the scatter plot of main effects showing how the total particle count varies with different levels for each experimental factor. The total particle counts are the average of two replicate values. For the most part, the range of total particle counts are similar for all factors and all levels. However, total particle count from C10 configuration shows up as an outlier in all cases. Additionally, particle counts for the ‘far’ level for the port distance factor are noticeably lower than the other cases, indicating that the Distance factor (X3) is likely an important factor affecting the total particle count or the factor that affects the exposure level.

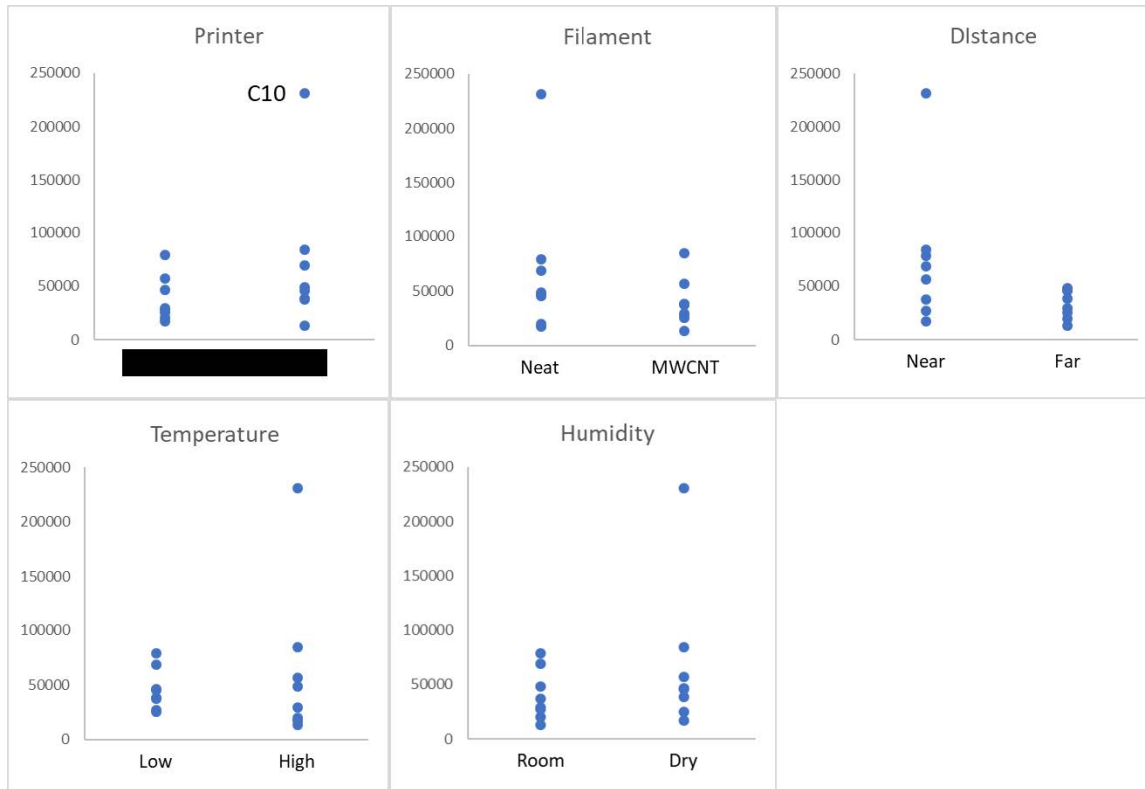


Figure 32: Scatter plots of total particle counts for the different settings for each experimental factor.

Main effects plot shown in Figure 33 is used to determine the ranked list of the factors and whether there is a dominant factor that influences the total particle count. Here, average total particle count for each level of a factor is plotted for all factors. For example, for factor X1 (printer model), the average of total particle counts for Printer 1 (- level) and the average of total particle counts for Printer 2 (+ level) are the two values for the X1: Printer plot. The effect of factor X1 is the difference between the average total particle counts. From the main effects plot, experimental factors can be ranked in the following order:

1. X3 – sampling port distance from the extrusion nozzle
2. X1 – printer model
3. X2 – filament type
4. X5 – filament storage condition
5. X4 – extrusion temperature

Clearly, the dominant factor is X3. Total particle counts increase when the distance between the sampling port and the extrusion nozzle decreases. This agrees with our assumption that sampling is more effective when the sampling nozzle is closer to the source of particles. X1 and X2 effects are also significant, and it is most likely that these factors interact strongly to influence the total particle counts. According to the main effects plot, printing with Printer 2 results in higher total particle counts on average. Similarly, printing with neat ABS filaments,

printing at higher extrusion temperature, and storing filaments in dry environment also results in higher total particle counts.

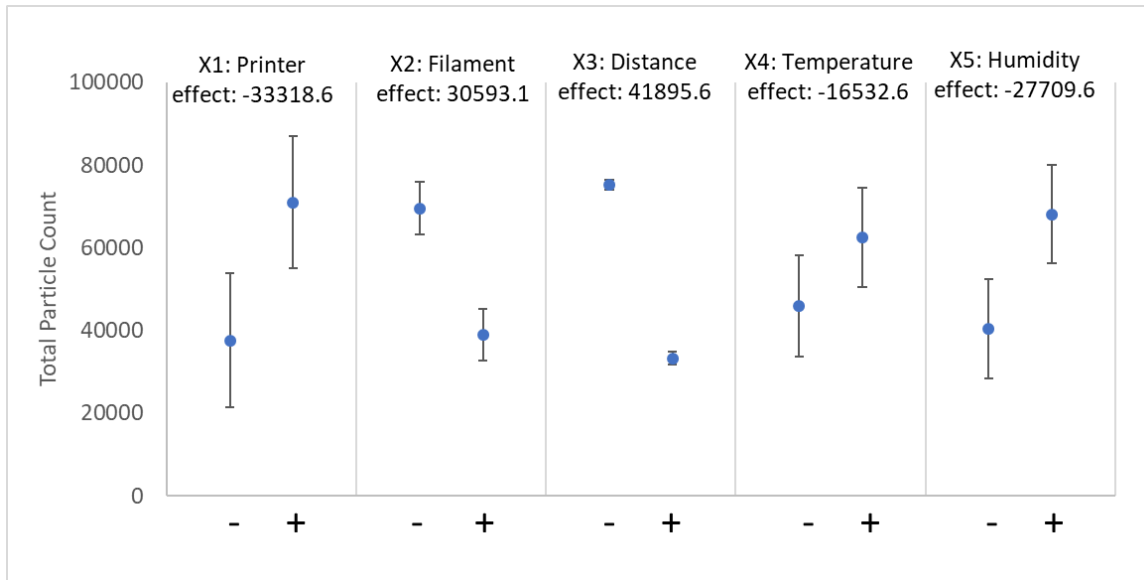


Figure 33: Main effects plot showing the average particle counts for each level of each factor. See Table 3 for the level assignments for each factor.

Although X3, X1, and X2 are the main factors affecting the total particle counts, uncertainty associated with these factors should be considered. Figure 34 is the main effect values plotted with uncertainties. Here, because of the large differences in the replicate 1 and replicate 2 results for the X1 factor, the X1 effect could be deemed negligible if the uncertainty for X1 effect is considered and factors X3 and X2 are the only factors showing significant effects. Although the uncertainties in main effects are not considered in the subsequent analysis, we should keep them in mind when interpreting effects of various factors.

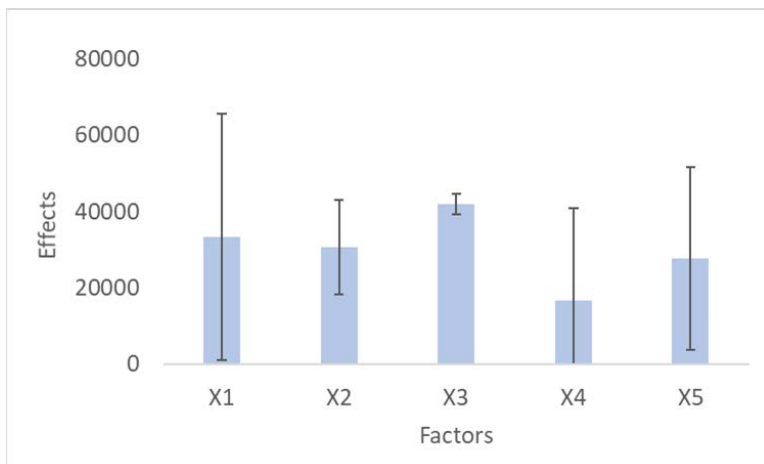


Figure 34: Main effects plot showing uncertainty associated with each effect.

Following the main effects analysis, full two factor interaction effects for all five factors were examined. We found that X3 and X4 effects were confounded with some of the interaction effects, probably because we utilized three factor interaction term $X3*X4*X5$ for blocking scheme for our 2^{3-1} fractional factorial design. Limiting our interaction effects analysis to three main factors identified earlier (X1, X2, and X3), we determined that interaction between factors X1 and X3 ($X1*X3$) and interaction between factors X1 and X2 ($X1*X2$) have significant effects on the total particle counts.

Figure 35 is the interaction plot matrix showing two factor interactions between factors X1, X2, and X3 and corresponding effect values. Dotted gray line is the mean total particle counts from all sample runs. Unlike main effects, interaction effects are difficult to interpret and the relationship between the factors are not obvious. We determined that the $X1*X3$ and $X1*X2$ are the two significant interactions that affect the total particle counts. According to the $X1*X3$ plot, the combination of Printer 1 and far sampling port ($X1-*X3+$) or Printer 2 and near sampling port ($X1+*X3-$) produces higher total particle counts compared to Printer 1 and near sampling port ($X1-*X3-$) or Printer 2 and far sampling port ($X1+*X3+$). This interaction effects can be interpreted as the combination of Printer 2 and near sampling port increases the total particle count more effectively than the mitigating effect of near sampling port on low particle count from Printer 1 printing. Similarly, $X1*X2$ plot indicates that the combination of Printer 1 and MWCNT ABS filament or Printer 2 and neat ABS filament results in higher total particle counts compared to Printer 1 and neat ABS filament or Printer 2 and MWCNT ABS filament.

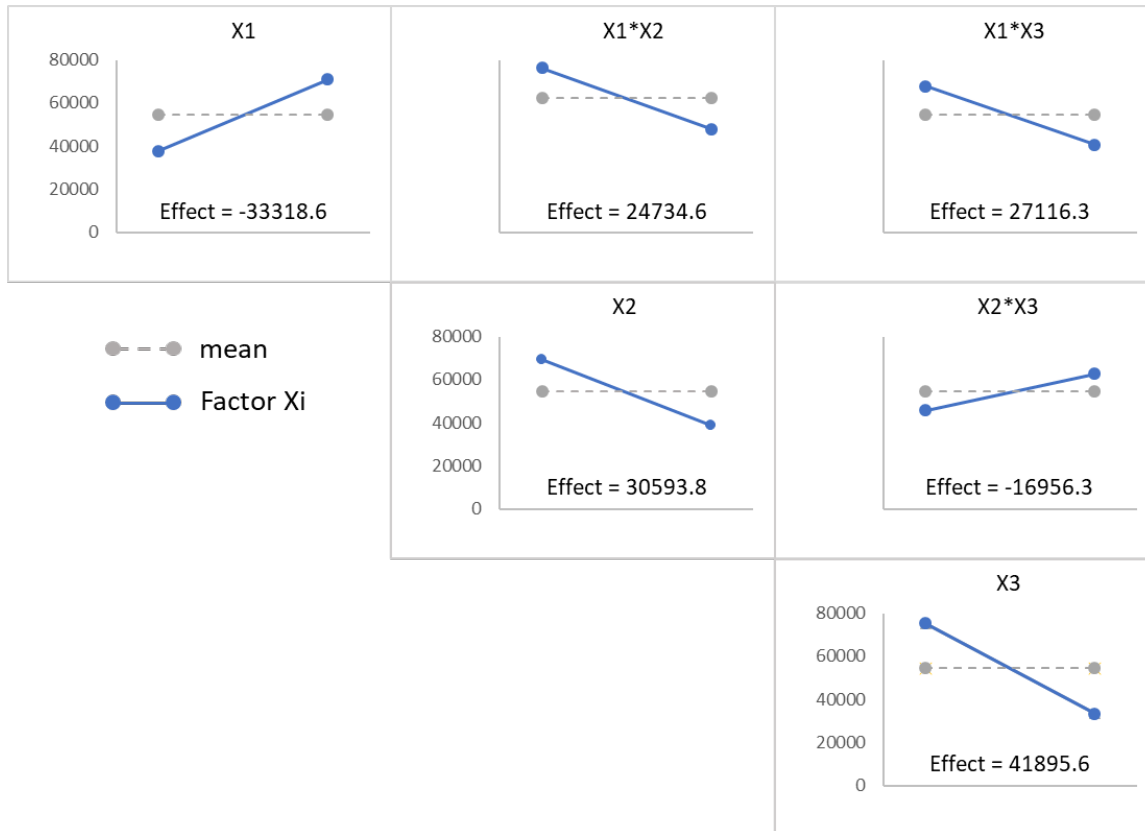


Figure 35: Two factor interaction plots for the three major factors X1, X2, and X3.

10 CONCLUSIONS

In this study, we carried out a five factor, two level fractional factorial experiments in two replicates to determine what factors influence the overall particle release behavior during 3D printing process using MWCNTs. To this end, we fabricated two 3D printing chambers and used them to sample particles released during 3D printing using two different 3D printers (X1). Four additional experimental factors likely to affect particle release during 3D printing were also considered. They were: 3D printing filament type (X2), sampling distance (X3), printing temperature (X4), and filament storage condition (X5).

Air sampling of particles released during 3D printing of a test object was performed in a randomized run order at different combinations of experimental factor settings. Particles collected onto silicon wafers using an electrostatic precipitator were imaged using an SEM. SEM imaging was performed with two goals in mind: 1) to detect and characterize individual MWCNTs by high resolution SEM imaging and 2) to survey a sufficiently large area of the silicon wafer to obtain statistically relevant particle population information. While we did not detect any individual MWCNTs, we did find many particles containing MWCNTs. To address the second goal, each silicon wafer was imaged using large area tile imaging routine, tile images

were processed and segmented for particles, and detected particles were analyzed for size distribution and number concentration of the respirable fraction of aerosolized particles greater than 130 nm and less than 10 μm in diameter.

We compared the particle size distributions from different experimental configurations but found that the particle size distributions were generally comparable with one another. All size distribution curves showed a main peak at ~ 300 nm and most of the released particle had diameters less than 2 μm . However, several experimental configurations did show a noticeable secondary peak in the size distribution. C06, C09, and C10 results showed a major peak around 300 nm and another one around 500 nm in both replicates. C01 and C02 also showed small secondary peaks in addition to the main peak at 300 nm. However, these results are only seen in one of the replicates.

In C09 and C10 configurations, particles were sampled close to the extrusion nozzle while printing with neat ABS filament on Printer 2. In C01 and C02, particles were sampled close to the extrusion nozzle while printing with neat ABS filament on Printer 1 and in C06, particles were sampled close to the extrusion nozzle while printing with MWCNT ABS filament on Printer 1. Printing temperature and filament storage humidity were different in these cases. The common factor, based on the description of the experimental configurations, seems to be the distance between the extrusion nozzle and the sampling port. However, not all configurations with 'near' setting for the sampling distance showed the secondary peak, indicating that there are other confounding factors.

The plot of total particle counts did not show any obvious trend. Consistency between replicates were relatively poor and, in some cases, total particle counts from blank runs were comparable to those from the sample runs. However, it did highlight that the total particle counts from C10 configuration were unusually high compared to the other results.

To determine the factors that impact the release, we used the total particle counts from each silicon wafer as our response variable. Main effects plot showed that factor X3, the distance between the extrusion nozzle and the sampling port, has the largest effect on the total particle counts. This is followed by printer model (X1) and filament type (X2). Examination of the two factor interaction effects showed that the interaction between the printer model and distance (X1*X3) and printer model and filament type (X1*X2) are relevant factors. The factors that affect the total particle counts are, in the order of their importance,

1. X3, Distance between the extrusion nozzle and sampling port
2. X1, Printer model
3. X2, Filament type
4. X1*X3, Interaction between printer model and distance

5. X1*X2, Interaction between printer model and filament type

In general, close distance, Printer 2, and neat ABS filaments are the conditions (levels) that resulted in increased total particle counts. Interaction effects were more complicated. Large discrepancies between replicate run results and confounding effects due to the use of blocking scheme in our fractional factorial design made interaction effects difficult to interpret.

The main goal of this study was to determine the factors that affect the size distribution of the particles that are released, or the total number of particles released during the printing process. However, one of the factors, X3 - distance between the particle source (printer extrusion nozzle) and the sampling port, is not a factor that affects the release process but the sampling of the release particles. Even if a specific configuration (printer, filament, printing temperature, and filament condition) greatly increase the total number of particle released, sampling conditions can affect the final particle count in our experiment. In other words, sampling port distance is the dominant factor in our study as shown in our effects analysis. In this study, we considered the distance between the sampling port and the source as a term that mimic exposure level. Because of this, it should be noted that the low particle count does not necessarily indicate low particle release. Rather it implies low exposure condition.

As mentioned earlier, identifying and interpreting relevant interaction effects was challenging. Although significant effort was made to remove systematic bias or trend through randomized run orders and control runs, consistency between replicate runs were poor in many cases. Although we have identified X3 as the dominant factor and, in general, neat ABS filaments result in larger total particle counts, the effects of printer model or the interaction between the filaments and port locations are not as clear cut.

To summarize, the following are the main conclusions:

- Sampling location has the greatest effect on the total particle counts. In general, sampling closer to the particle source resulted in higher total particle count. However, it should be noted that there is an optimal distance. Our preliminary sampling runs showed that sampling within few mm of the source is not as efficient as sampling about 25 mm away from the source.
- Neat ABS filament produced more particles of respirable size than MWCNT ABS filament during 3D printing.
- Printing temperature, for the ranges of temperature tested in this study, did not have much effect on the total particle counts.
- All experimental conditions produced similar particle distribution with a single major peak around 300 nm. There were several conditions where a smaller secondary peak was seen at 500 nm or 700 nm. Although 4 out of 5 instances, the secondary peak was detected when

neat ABS filament was used, there was no simple relationship between the appearance of the secondary peak and the main experimental factors.

- Humidity effects were difficult to determine because of the confounding of factors stemming from the blocking scheme used in our fractional factorial design.
- Most of the particles sampled were less than 2 μm in diameter. There were also particles greater than the respirable particle size range of 10 μm but these were not as plentiful as the smaller particles. It should be noted that the range of sampled particle size depends on the sampling method and should not be confused with the range of released particle size.
- Many of the particles sampled during the MWCNT ABS filament printing were found to contain MWCNTs. Some particles had smooth surfaces and most MWCNTs were embedded within the particles. Some particles had irregular morphologies with protruding MWCNTs covering the particle surface. However, most of the particles containing MWCNTs were greater than 2 μm in diameter although some MWCNT containing particles as small as 150 nm were seen.

Although we were able to identify a couple of main factors that affect the total particle counts, large discrepancies between replicates and confounding effects made it difficult to assess more nuanced interaction effects between factors. For the next phase of this study, we will need to reduce the measurement uncertainty by increasing the number of replicates or replicate consistency. We also need to determine the relationship between particles released and particles sampled with respect to concentration and size range to understand hazards associated with the 3D printing process. This will require a control MWCNT aerosol source which is well-defined and uniformly dispersed. Although there are many methods for testing particle sampling efficiency using polymer beads or other spherical particles, currently we do not have a method to consistently disperse MWCNTs and use it to characterize the performance of different sampling methods. Our next effort will focus on developing a method to generate robust and well characterized MWCNT control dispersion.

ACKNOWLEDGEMENT

We thank James Filliben for the factorial design of the 3D printing experiments and David Goodwin for the TGA analysis of the 3D filaments.

ABBREVIATIONS & TERMS

ABS: Acrylonitrile butadiene styrene

ATR: attenuated total reflection

ETD: Everhart-Thronley detector

FTIR: Fourier transform infrared
HEPA: high efficiency particulate air
HFW: horizontal field width
HIPS: high impact polystyrene
MOUDI: micro-orifice uniform deposit impactor
MWCNT: multi-walled carbon nanotube
NAS: nanometer aerosol sampler
PC: polycarbonate
PETG: polyethylene terephthalate glycol
PLA: polylactic acid
SE: secondary electron
SEM: scanning electron microscope
TGA: thermal gravimetric analysis
TLD: through-the-lens detector
WD: working distance

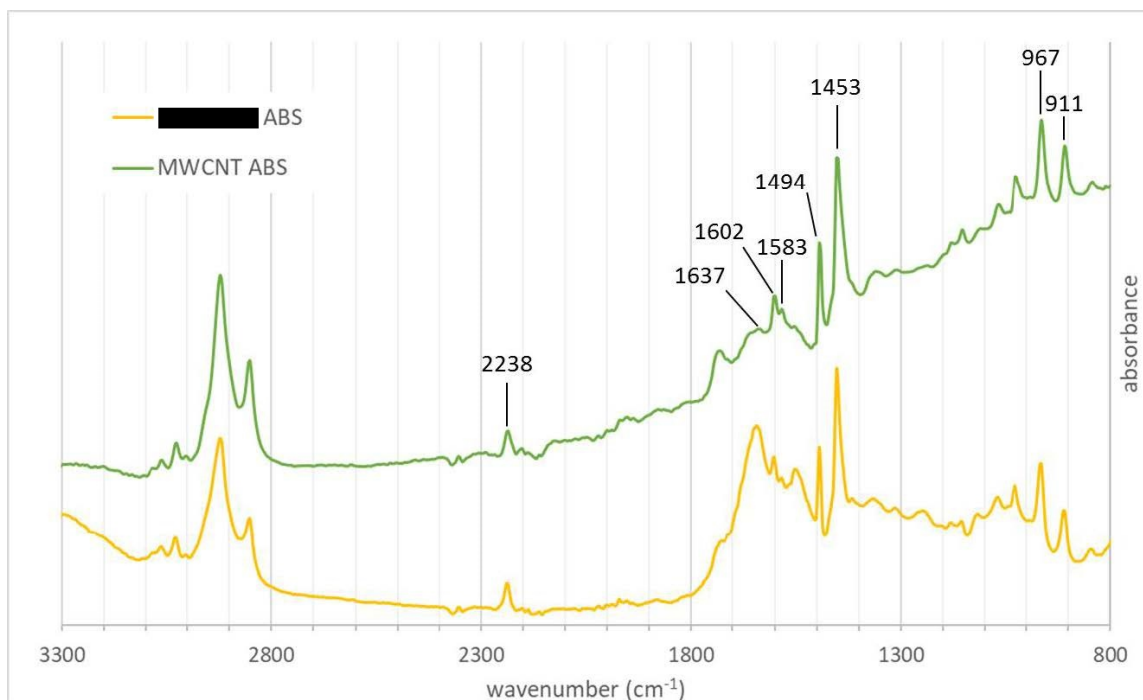
REFERENCES

1. <https://www.forbes.com/sites/louiscolombus/2015/03/31/2015-roundup-of-3d-printing-market-forecasts-and-estimates/#11c01fac1b30>. “2015 Roundup of 3D Printing Market Forecasts and Estimates.”
2. The National Nanotechnology Initiative Report “Environmental, Health, and Safety Research Needs for Engineered Nanoscale Materials”, September 2006.
3. <http://industryarc.com/Report/15312/3d-printing-metal-market.html> “3D Printing Metals Market Analysis: By State (Powder, Filament and Others); By Metal Type (Titanium, Nickel, Stainless Steel, Aluminum and Others); By Application (Medical, Automotive, Aerospace and Defense and Others) – With Forecast (2016-2021)”
4. <http://www.prnewswire.com/news-releases/global-3d-printing-materials-market-for-electronics--consumer-products-automotive-medical-industrial-education-aerospace-and-other-applications---forecasts-to-2020-300007788.html> “Global 3D Printing Materials Market for Electronics & Consumer Products, Automotive, Medical, Industrial, Education, Aerospace and Other Applications - Forecasts to 2020”
5. NIOSH (2013) “Occupational Exposure to Carbon Nanotubes and Nanofibers”. Cincinnati, OH: U.S. Department of Health and Human Services, Centers for Disease Control and Prevention, National Institute for Occupational Safety and Health, DHHS (NIOSH) Publication No. 2013-145.
6. Desrousseaux, C., Cueff, R., Aumeran, C., Garrait, G., Mailhot-Jensen, B., Ousmane Traoré, O. & Sautou, V. (2015) “Fabrication of Acrylonitrile-Butadiene-Styrene Nanostructures with Anodic Alumina Oxide Templates, Characterization and Biofilm Development Test for Staphylococcus Epidermidis” PLOS One, DOI:10.1371/journal.pone.0135632.
7. Scott, K. (2015) “Exposure Assessment of Carbon Nanotubes (CNTs) in CNT enhanced Fibers and Textiles in Children’s Products”, Gaithersburg, MD: National Institute of Standards and Technology, NIST ROA # 643-15-41.
8. Lee, K.W. & Mukund, R. (2001) “Filter Collection” In Baron, P.A. & Willeke, K (Eds.), “Aerosol Measurement”, 2nd Ed. (pp. 197 – 228). Toronto, Canada, Wiley-Interscience.
9. Goldstein, J., Newbury, D., Joy, D., Lyman, C., Echlin, P., Lifshin, E., Sawyer, L. & Michael, J. “Scanning Electron Microscopy and X-Ray Microanalysis”, 3rd Ed. (2003) Springer, N.Y. p 199.
10. Petersen, E.J., Lam, T., Gorham, J.M., Scott, K.C., Long, C.L., Stanley, D., Sharma, R., Liddle, J.A., Pellegrin, B. and Nguyen, T. (2014) “Methods to assess the impact of UV irradiation on the surface chemistry and structure of multiwall carbon nanotube epoxy nanocomposites” Carbon **69**, 194-205.
11. NIST Additive Manufacturing Test Artifact, <https://www.nist.gov/el/intelligent-systems-division-73500/production-systems-group/nist-additive-manufacturing-test>, last accessed January 7, 2018.

12. Particulate Matter (PM) Basics, <https://www.epa.gov/pm-pollution/particulate-matter-pm-basics>, last accessed January 7, 2018.
13. Schindelin, J., Arganda-Carreras, I., Frise, E., Kaynig, V., Longair, M., Pietzsch, T., Preibisch, S., Rueden, C., Saalfeld, S., Schmid, B., Tinevez, J.Y., White, D.J., Hartenstein, V., Eliceiri, K., Tomancak, P. & Cardona, A. (2012), "Fiji: an open-source platform for biological-image analysis", *Nat. Methods* **9(7)**, 676-682.
14. Izenman, A.J., "Modern Multivariate Statistical Techniques" (2008) Springer, N.Y. p 58.

APPENDIX 1: FTIR SPECTRA OF ABS FILAMENTS

FTIR spectra (run in ATR mode) of representative materials. The MWCNT ABS spectrum is of the MWCNT ABS filament employed in the current study. The Manufacturer 2 ABS spectrum is of an ABS filament from another filament manufacturer. Literature showed comparable absorption frequencies confirming ABS as the matrix material for both samples (Desrousseaux et al. *PLOS One* 2015).



- CN stretching from acrylonitrile at 2238 cm⁻¹
- C = C stretching mode of poly(butadiene) at 1637 cm⁻¹
- aromatic ring in styrene at 1602 cm⁻¹, 1583 cm⁻¹ and 1494 cm⁻¹
- scissoring mode of the CH₂ groups at 1453 cm⁻¹
- C-H deformation for hydrogen atoms attached to alkenic carbons in poly(butadiene) at 967 cm⁻¹ and 911 cm⁻¹

APPENDIX 2: MWCNT NANOCOMPOSITE IMAGES

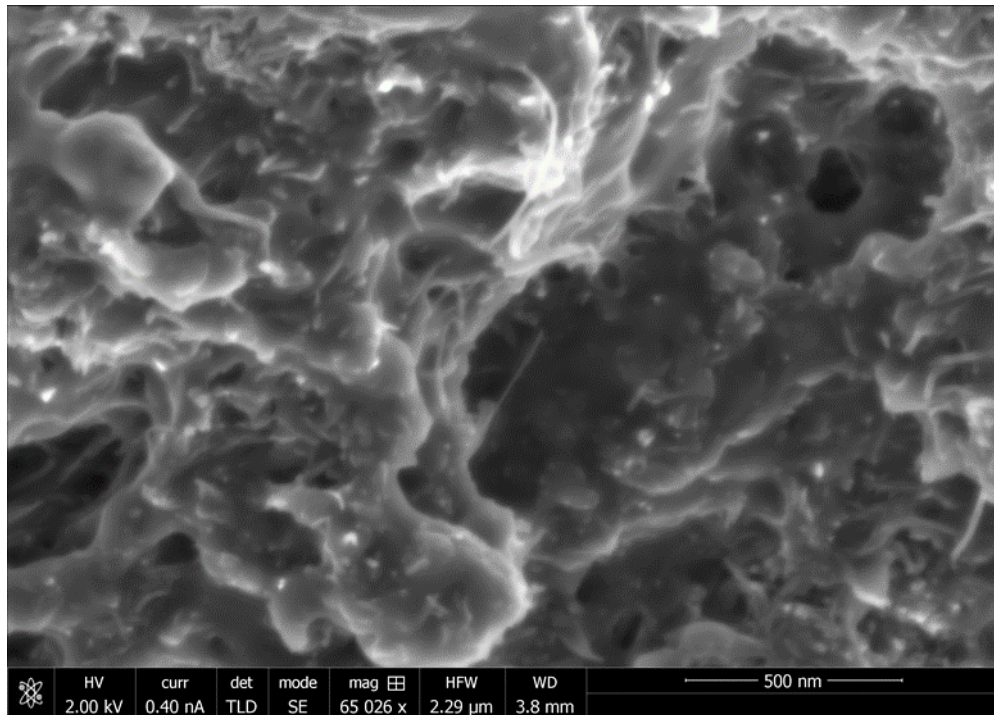


Figure A2.1: SEM image of MWCNT epoxy nanocomposite sample showing subsurface MWCNTs and protruding MWCNTs. The nanocomposite sample was made in-house with 5 % mass fraction of MWCNT. The presence of MWCNTs was confirmed using subsequent Raman spectroscopy and TEM imaging.

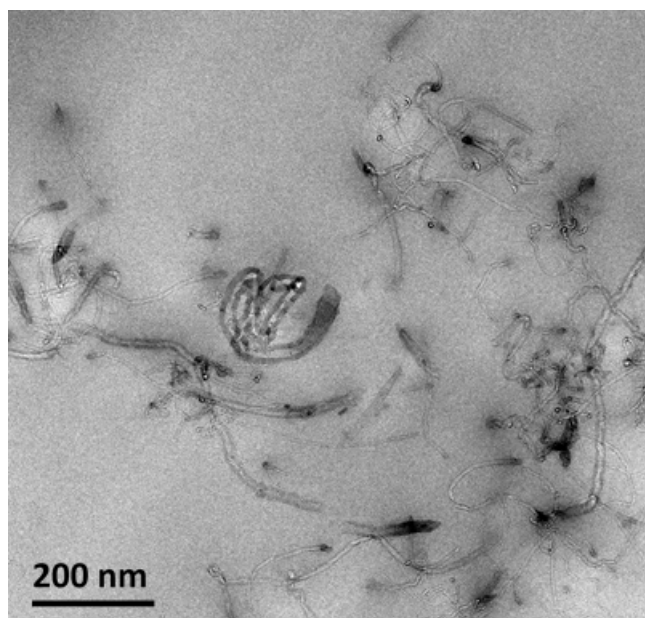


Figure A2.2: TEM image of ultramicrotome section of MWCNT epoxy nanocomposite sample showing multiwall structure of MWCNTs embedded in the epoxy matrix.

APPENDIX 3: FRACTIONAL FACTORIAL DESIGN MATRIX FOR SINGLE REPLICATE

| X1 | X2 | X3 | X4 | X5 |
|----|----|----|----|----|
| - | - | - | - | + |
| - | - | - | + | - |
| - | - | + | - | - |
| - | - | + | + | + |
| - | + | - | - | + |
| - | + | - | + | - |
| - | + | + | - | - |
| - | + | + | + | + |
| + | - | - | - | + |
| + | - | - | + | - |
| + | - | + | - | - |
| + | - | + | + | + |
| + | + | - | - | + |
| + | + | - | + | - |
| + | + | + | - | - |
| + | + | + | + | + |

APPENDIX 4: 3D PRINTER CHAMBER CLEANING PROTOCOL

1. Wipe down inner surfaces of printer, including build plate and frame, using polyester wipes (TX 1009 AlphaWipe, Texwipe, Kernersville, NC) and isopropyl alcohol.
2. Use HEPA-equipped vacuum to clean printer area and nooks and crannies.
3. Using the wipes and isopropyl alcohol, wipe down surfaces of enclosure, including positioning arm and surface of nanometer aerosol sampler (NAS).
4. Blow out inside of sampling tube with compressed air.
5. Wipe down inner chamber of NAS.
6. When changing filaments, extrude the new filament for at least 3 minutes to cycle out previous filament from the nozzle.
7. Leave chamber door open with the large air filter on for at least 10 minutes between each run.

APPENDIX 5: SEM IMAGING PARAMETERS

For MAPS tile images the following parameters were used:

- Frame resolution = 3072 x 2048
- Map dimensions = 50 x 50 = 2500 tiles
- Total map width = 18.04 mm
- Focus = fixed, 4 mm working distance (WD)
- HFW = 400 μm
- Pixel = 130.2 nm
- Dwell time = 1 μs
- Tile overlap = 10 % (x and y)
- Run duration = ~10 hrs

For low resolution survey images and tile images, the following settings were used:

- SEM Mode 1 (non-immersion)
- Detector: Everhart-Thornley Detector (ETD)
- Horizontal Field Width (HFW): 400 μm
- Resolution: 3072 x 2048
- Dwell time: 1 μs
- Fixed focus at WD = 4 mm
- Beam Energy: 3 keV
- Beam Current: 0.10 nA

For high resolution images, the following settings were used:

- SEM Mode 2 (immersion mode)
- Detector: through-the-lens detector (TLD)
- Horizontal Field Width (HFW): 33.5 μm
- Resolution: 3072 x 2048
- Dwell time: 3 μs
- Manually focused
- Beam Energy: 3 keV
- Beam Current: 0.10 nA

APPENDIX 6: RANDOMIZED WAFER IMAGING ORDER

| Week (4) | Image Session | Image Date | Run (32) | Config |
|-------------|---------------|------------|-------------|--------|
| 1 | 1 | 03/27/17 | 30 | C12-R2 |
| 1 | 2 | 03/28/17 | 8 | C02-R1 |
| 1 | 3 | 03/29/17 | 14 | C07-R1 |
| 1 | 4 | 03/30/17 | 20 | C02-R2 |
| 2 | 5 | 04/03/17 | 10 | C04-R1 |
| 2 | 6 | 04/04/17 | 22 | C16-R2 |
| 2 | 7 | 04/05/17 | 26 | C13-R2 |
| 2 | 8 | 04/06/17 | 4 | C16-R1 |
| 3 | 9 | 04/17/17 | 29 | C08-R2 |
| 3 | 10 | 04/18/17 | 12 | C15-R1 |
| 3 | 11 | 04/19/17 | 3 | C03-R1 |
| 3 | 12 | 04/20/17 | 17 | C05-R2 |
| 4 | 13 | 05/01/17 | 23 | C11-R2 |
| 4 | 14 | 05/02/17 | 15 | C06-R1 |
| 4 | 15 | 05/03/17 | 7 | C14-R1 |
| 4 | 16 | 05/04/17 | 25 | C03-R2 |
| 5 | 17 | 05/15/17 | 31 | C10-R2 |
| 5 | 18 | 05/16/17 | 24 | C07-R2 |
| 5 | 19 | 05/17/17 | 16 | C12-R1 |
| 5 | 20 | 05/18/17 | 5 | C08-R1 |
| 6 | 21 | 05/22/17 | 11 | C01-R1 |
| 6 | 22 | 05/23/17 | 28 | C01-R2 |
| 6 | 23 | 05/24/17 | 2 | C05-R1 |
| 6 | 24 | 05/25/17 | 19 | C14-R2 |
| 7 | 25 | 06/06/17 | 6 | C09-R1 |
| 7 | 26 | 06/07/17 | 21 | C04-R2 |
| 7 | 27 | 06/08/17 | 9 | C13-R1 |
| 7 | 28 | 06/09/17 | 18 | C09-R2 |
| 8 | 29 | 06/12/17 | 27 | C15-R2 |
| 8 | 30 | 06/13/17 | 13 | C10-R1 |
| 8 | 31 | 06/15/17 | 32 | C06-R2 |
| 8 | 32 | 06/16/17 | 1 | C11-R1 |

APPENDIX 7: FIJI SCRIPTS

MAPSPro.ijm

```
// Asks for the top level image directory and processes all the directory in
it.
//
// NOTE
// this assumes you want to process all images in your input image directory.
// still needs some error handling code.
//
// Keana Scott
// 2017-09-10

dataDir=getDirectory("Choose the top level input image directory");
dlist = getFileList(dataDir);
n = dlist.length;
procDir=getDirectory("Choose the top level processed image directory");

setBatchMode(true);

// for each folder
//   create a processed folder
//   for each image
//     crop the image to remove the overlapped region.  We will miss the
strips on top and left.
//     perform processing on cropped image
//       run 'analyze particles'
//       save binary image
//     close open windows
// save accumulated particle analysis results to a txt file

for (i=0; i<n; i++) { // for each folder
  imgDir=dataDir+dlist[i];
  flist=getFileList(imgDir);
  m=flist.length;
  outDir=procDir+dlist[i];
  folder = substring(dlist[i],0,lengthOf(dlist[i])-1);
//   print(folder);
  if (File.isDirectory(imgDir)) { // make the proc folder
    File.makeDirectory(outDir);
// clear the results buffer
// B/C autocorrect
// median filter
// thresh
// median filter
// binary
// fill holes
    run("Clear Results");
    for (j=0; j<m; j++){
      open(imgDir+flist[j]);
      bin=getImageID();
      selectImage(bin);
      fname=getInfo("image.filename");
      if (matches(fname, ".*Tile.*")) {
```

```

        if (j==0){
        h=getHeight();
        w=getWidth();
        h10=h-floor(0.1*h);
        w10=w-floor(0.1*w);
        }
        run("Specify...", "width=2765 height=1843 x=307 y=205");
        run("Crop");
run("Smooth");
run("Enhance Contrast", "saturated=0.35");
setOption("BlackBackground", false);
setAutoThreshold("Intermodes");
run("Convert to Mask", "method=Intermodes background=Light");
run("Median...", "radius=2");
run("Make Binary");
run("Fill Holes");
saveAs("tif", outDir+"bin-"+fname);
run("Set Scale...", "distance=0 known=0 pixel=1 unit=pixel");
run("Set Measurements...", "area shape redirect=None decimal=0");
run("Analyze Particles...", "size=0-Infinity circularity=0-1.00
show=Nothing display exclude");
        fname=substring(fname, 0, indexOf(fname, ".tif"));
        close("*.tif");
        }
        saveAs("Results", procDir+folder+".txt");
run("Clear Results");
close("Results");
    }
}
close();
exit();

```

MAPSPro-bin.ijm

```
//
// Run Analyze Particle routine but picks out the bad images.
//
// Keana Scott
// 2017-09-21

dataDir=getDirectory("Choose the top level input binary image directory");
dlist = getFileList(dataDir); // get the number of folders in the directory
n = dlist.length;

print(dlist[0])
setBatchMode(true);
//

// for each folder
//   create a processed folder
//   for each image
//     crop the image to remove the overlapped region. We will miss the
strips on top and left.
//     perform processing on cropped image
//     run 'analyze particles'
//     save binary image
//     close open windows
// save accumulated particle analysis results to a txt file

for (i=0; i<n; i++) { // for each binary image folder
  binDir=dataDir+dlist[i];
  // get the list of files in the current binary image directory
  flist=getFileList(binDir);
  m=flist.length; // get the number of files
  // get the name, not the full path, of the binary image directory
  folder = substring(dlist[i],0,lengthOf(dlist[i])-1);
  print(folder);
  if (File.isDirectory(binDir)) {
    run("Clear Results");
    rf = File.open(dataDir+folder+".txt");
    errcount = 0;
    err=newArray();
    //lastrow=0;
    for (j=0; j<m; j++){ // for each binary image in the current
folder
      open(binDir+flist[j]);
      bin=getImageID();
      selectImage(bin);
      fname=getInfo("image.filename");
      //print(fname);
      if (matches(fname, ".*bin-Tile.*")) { // do only if the image
filename contains 'bin-Tile'
        run("Set Scale...", "distance=0 known=0 pixel=1
unit=pixel");
        run("Set Measurements...", "area shape redirect=None
decimal=0");
        run("Analyze Particles...", "size=0-Infinity circularity=0-
1.00 show=Nothing display exclude");
```

```

        fname=substring(fname, 0, indexOf(fname, ".tif"));
        close("*.tif");
        print(nResults);
        if ((nResults > 0) && (nResults < 1000)) {
            for (row=0; row<nResults; row++) {
                a = getResult("Area", row);
                print(rf, a);}
            }
        else if (nResults >= 1000) {
            errcount = errcount + 1;
            err=Array.concat(err, fname);
            }
        run("Clear Results");
    }

}
File.close(rf);
run("Clear Results");
close("Results");
lf=File.open(dataDir+folder+".log");
for (nf=0; nf<errcount; nf++){
    print(lf, err[nf]);
}
File.close(lf);
}
}

close();
exit();

```